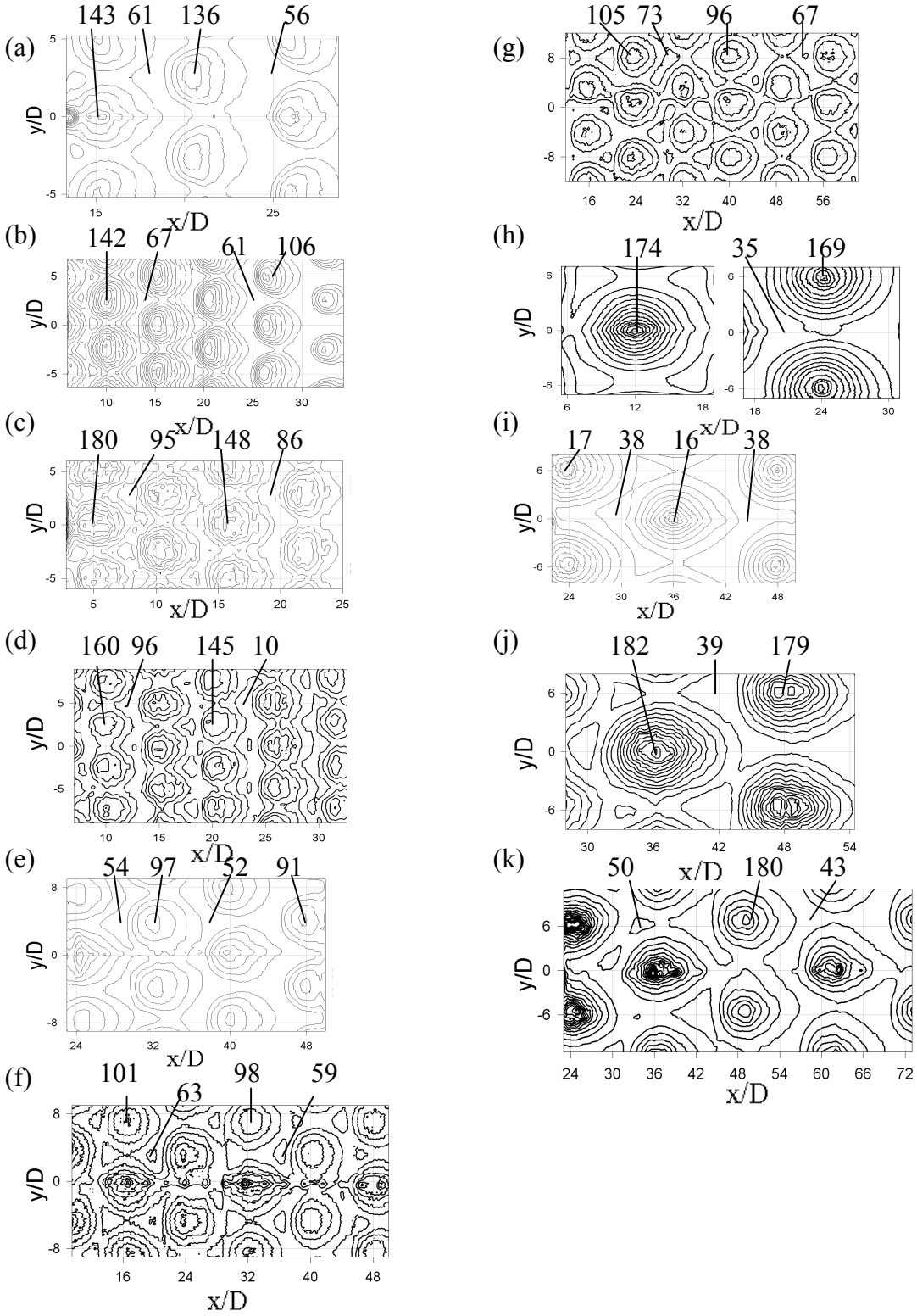

Figure 5.1. Spatially resolved distributions of surface Nusselt number for Re_j = 30000 with hole spacings and *Ma* values of: (a) 5*D* and *Ma* = 0.09, (b) 5*D* and *Ma* = 0.17, (c) 5*D* and *Ma* = 0.30, (d) 5*D* and *Ma* = 0.38, (e) 8*D* and *Ma* = 0.20, (f) 8*D* and *Ma* = 0.35, (g) 8*D* and *Ma* = 0.45, (h) 12*D* and *Ma* = 0.10, (i) 12*D* and *Ma* = 0.17, (j) 12*D* and *Ma* = 0.38, (k) 12*D* and *Ma* = 0.45.

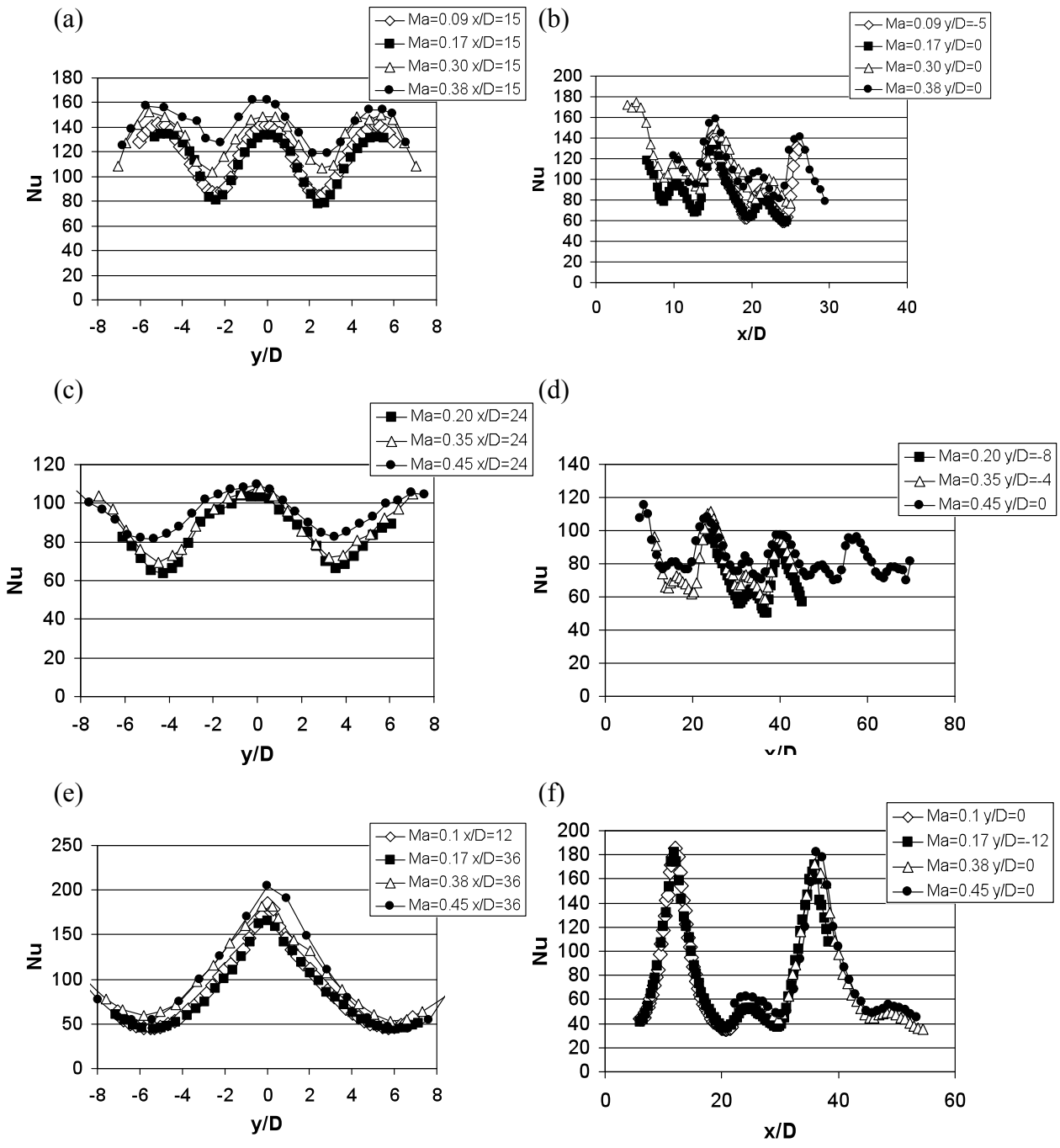

Figure 5.2. Local surface Nusselt number variations for Re_j = 30,000 and *Ma* values of 0.1, 0.2, 0.35, and 0.45: (a) hole spacing 5*D* spanwise variations, (b) hole spacing 5*D* lengthwise variations, (c) hole spacing 8*D* spanwise variations, (d) hole spacing 8*D* lengthwise variations, (e) hole spacing 12*D* spanwise variations, (f) hole spacing 12*D* lengthwise variations.

greatest for the hole spacing 5*D* and almost unnoticeable for the hole spacing 12*D*, indicating the increasing effect of spent air crossflow with decreasing hole spacing. This repeatability in the spanwise direction and decreasing *Nu* in the lengthwise direction follows the same trend seen in the incompressible test cases reported in Chapter 4. It is also noteworthy that there is a uniform increase in Nusselt number values with increasing Mach number for each of the three hole spacings.

Figure 5.3 presents Nusselt numbers which are line-averaged over *y/D* from –2.5 to +2.5 for a hole spacing of 5*D*, from -4.0 to +4.0 for a hole spacing of 8*D*, and from -6.0 to +6.0 for a hole spacing of 12*D*. Each of the three hole spacings shows considerable increase in Nusselt number with increasing Mach number and decreasing values with increasing *x/D*. This decrease with *x/D* is more pronounced for tighter hole spacings due to the increased effect of spent air crossflow. Like this local data, this is similar to the trends seen in the incompressible data for constant Mach number and increasing Reynolds number.

5.3 Local Area-Averaged Nusselt Number Variations With Mach Number

Figures 5.4-5.6 compare spatially averaged Nusselt numbers for hole spacings 5D, 8D and 12D with the Florschuetz et al. (1981) correlation values. Figure 5.4 shows the comparison for 5*D* hole spacing at constant Reynolds number 30,000 and Mach number values of 0.09, 0.17, 0.30, and 0.38. Here the two cases for $Ma \leq 0.2$ show good agreement with Florschuetz et al. (1981), with a departure from the correlation that increases with increasing Mach number. Figure 5.5 shows the comparison for 8*D* hole spacing at constant Reynolds number and Mach number values of 0.10, 0.20,

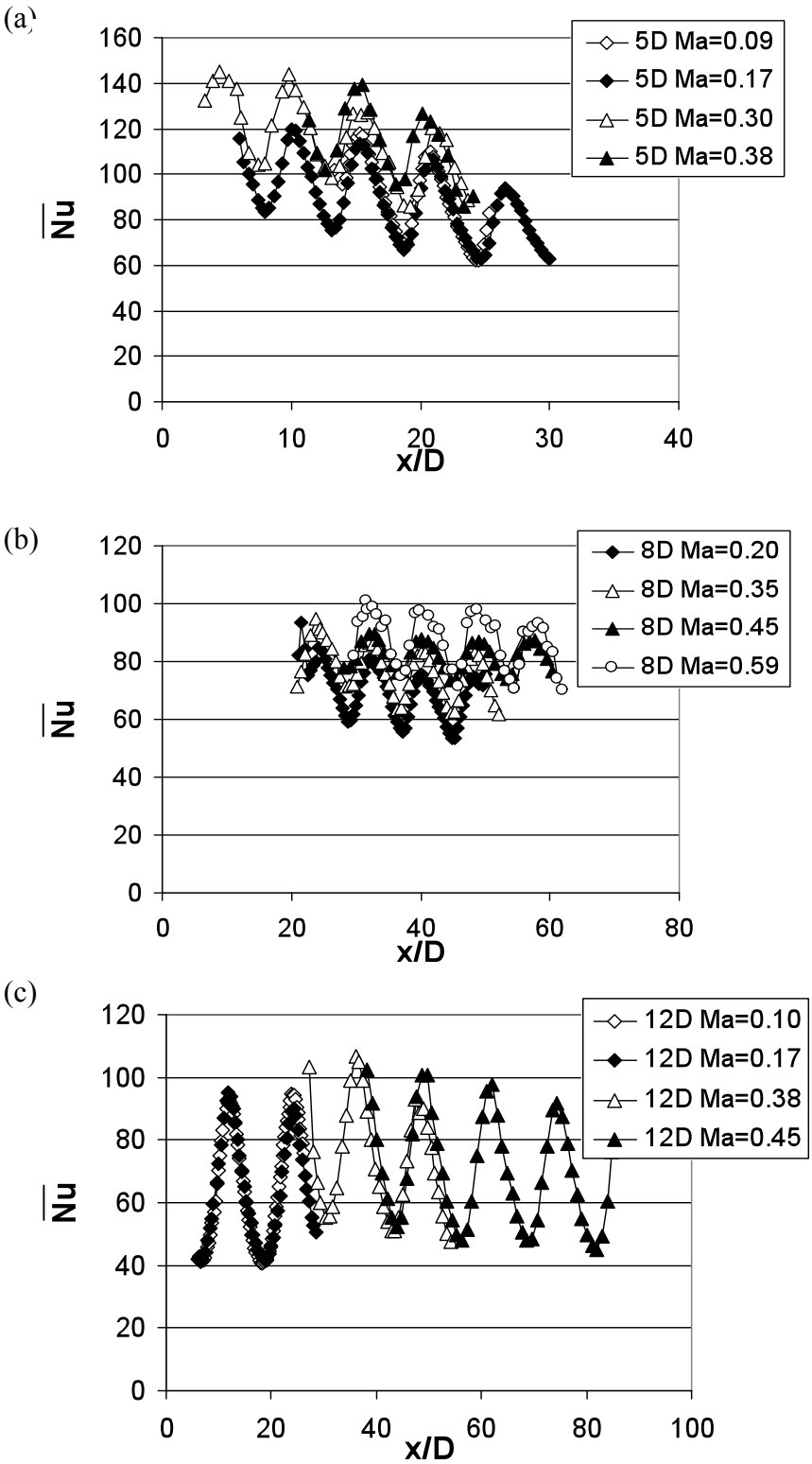

Figure 5.3. Surface Nusselt number variations which are line averaged over y/D for one hols spacing in either direction from the origin for constant Reynolds number 30,000 and (a) hole spacing 5*D Ma* = 0.09, 0.17, 0.30, and 0.38, (b) hole spacing 8*D Ma* = 0.20, 0.35, 0.45, and 0.59, (c) hole spacing 12*D Ma* = 0.10, 0.17, 0.38, and 0.45.

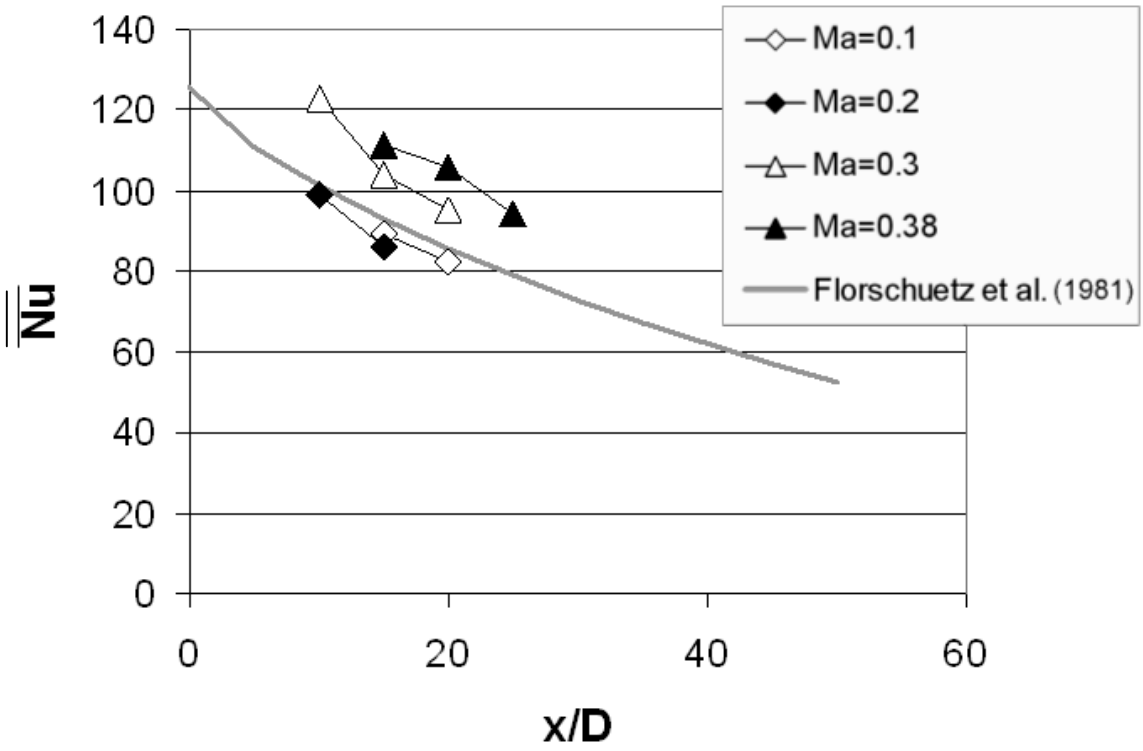

Figure 5.4. Hole spacing $X/D = Y/D = 5$ comparison of area average Nusselt numbers with correlation of Florschuetz et al. (1981) for $Re_j = 30{,}000$ and Ma values of 0.1, 0.17, 0.30, and 0.38.

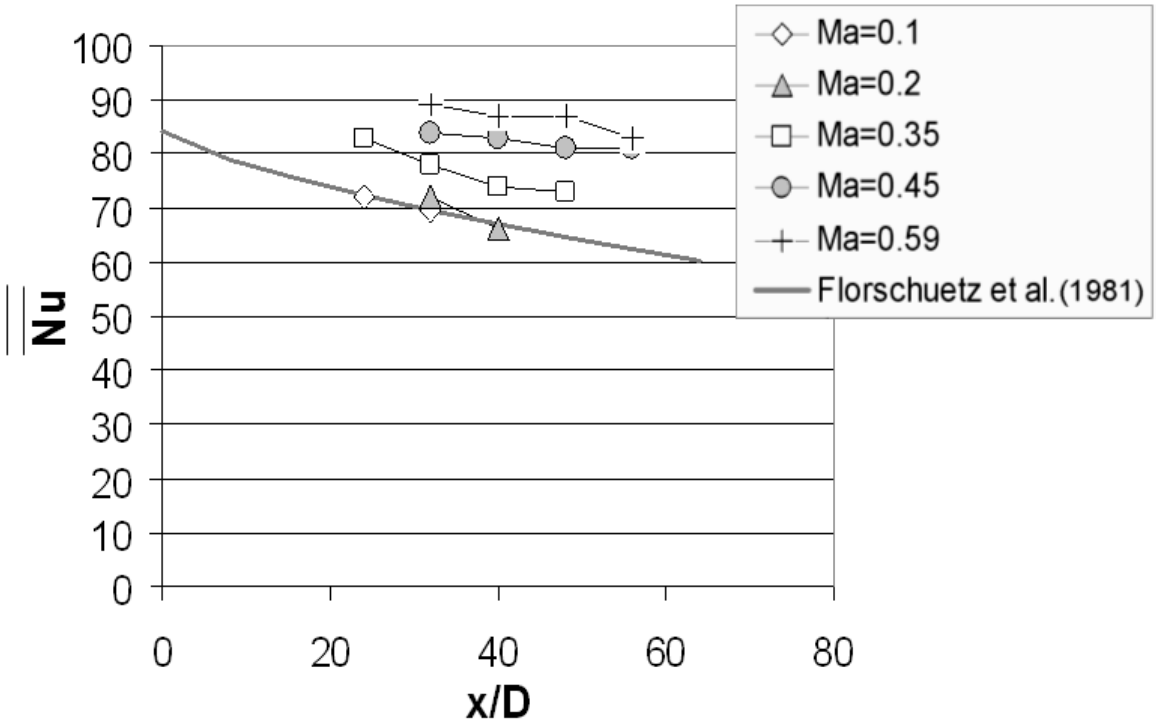

Figure 5.5. Hole spacing $X/D = Y/D = 8$ comparison of area average Nusselt numbers with correlation of Florschuetz et al. (1981) for Re_j = 30,000 and Ma values of 0.1, 0.2, 0.35, 0.45, and 0.59.

0.35, 0.45, and 0.59. Here, as seen for the 5*D* hole spacing data, the two cases for *Ma* ≤ 0.2 show good agreement with Florschuetz et al. (1981), with a departure from the correlation that increases with increasing Mach number. Figure 5.6 shows that for incompressible cases, the spatially averaged Nusselt number values are consistent with each other. The increase seen for the other two hole spacings with increasing Mach number is also present here. These results clearly show that Mach number has a significant impact on heat transfer for an array of impinging jets. It is therefore not reasonable to rely only on Nusselt number predictions based on correlations that neglect Mach number effect for cases where *Ma* ≥ 0.3.

As was previously noted in Chapter 4, the 12D hole spacing data are outside the range of applicability of the Florschuetz et al. (1981) correlation, which does not consider geometries with hole spacing greater than 8*D* for a staggered array. It is therefore not surprising that the incompressible data presented in Fig. 5.6 are slightly higher than correlation predicted values.

5.4 Local Area-Averaged Nusselt Numbers and Mach Number Correlation Equations

Existing correlations for arrays of impinging jets generally do not include compressible flow effects. To partially resolve this deficiency, spatially-averaged Nusselt numbers are compared to the correlation of Florscheutz et al. (1981) for Re_j = 30000 and values of Mach number that range from 0.1 to 0.45. Figure 5.7 shows the Mach number dependent deviation from the predicted Nu value for hole spacing *X/D* = *Y/D* = 5 while figs. 5.8 and 5.9 show this for hole spacings of *X/D* = *Y/D* = 8, and *X/D* = *Y/D* = 12 respectively. These data are given for specific x/D values, and for specific values of impingement Mach number.

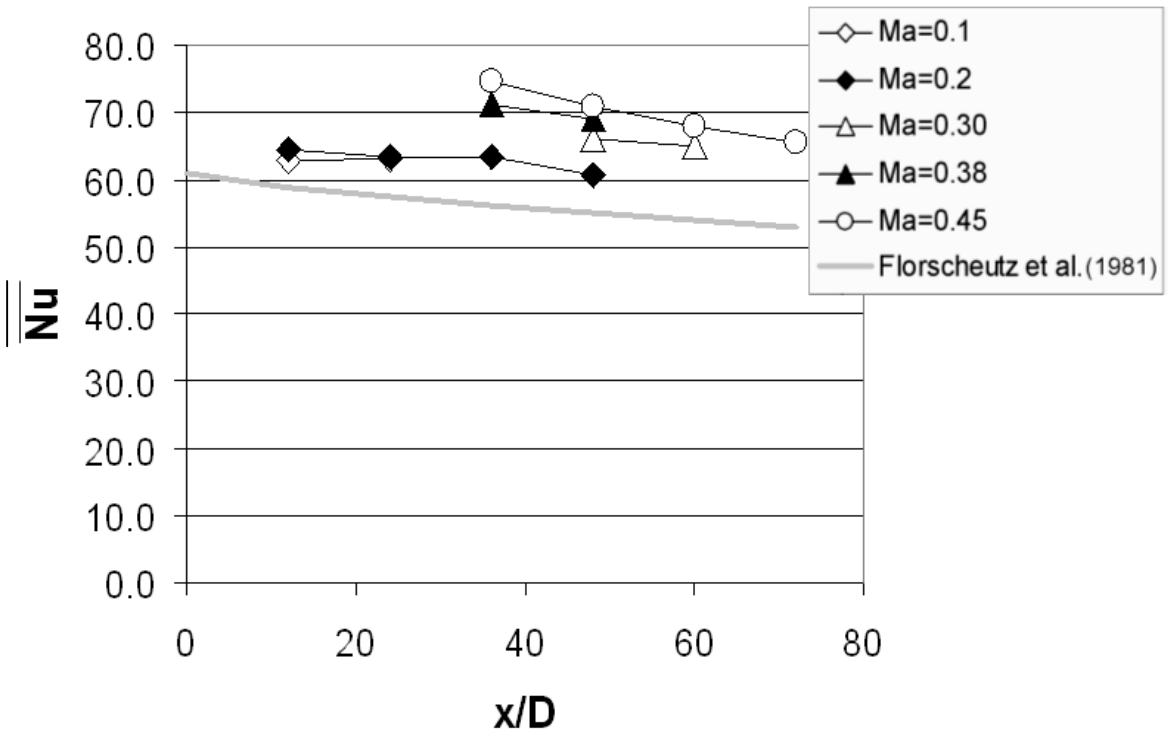

Figure 5.6. Hole spacing $X/D = Y/D = 12$ comparison of area average Nusselt numbers with correlation of Florschuetz et al. (1981) for $Re_j = 30{,}000$ and Ma values of 0.1, 0.2, 0.35, 0.38, and 0.45.

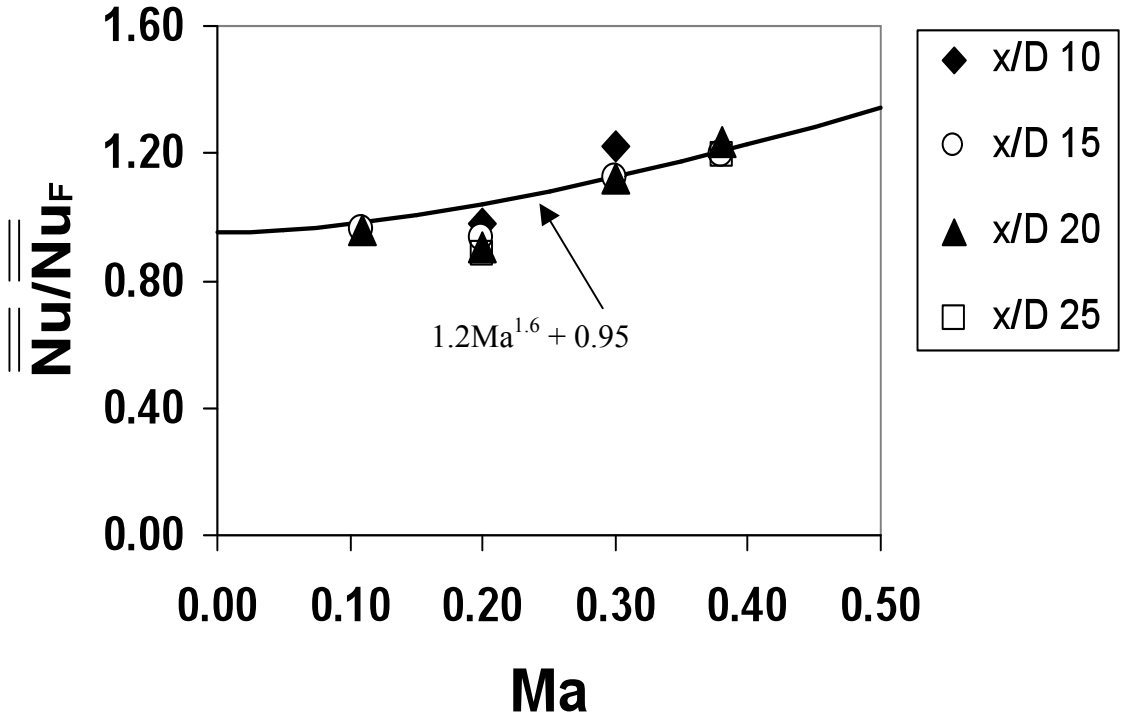

Figure 5.7. Nusselt number correlation with Mach number for hole spacing X/D = 5, Re_j = 30,000 and Ma values of 0.11, 0.20, 0.30, and 0.38.

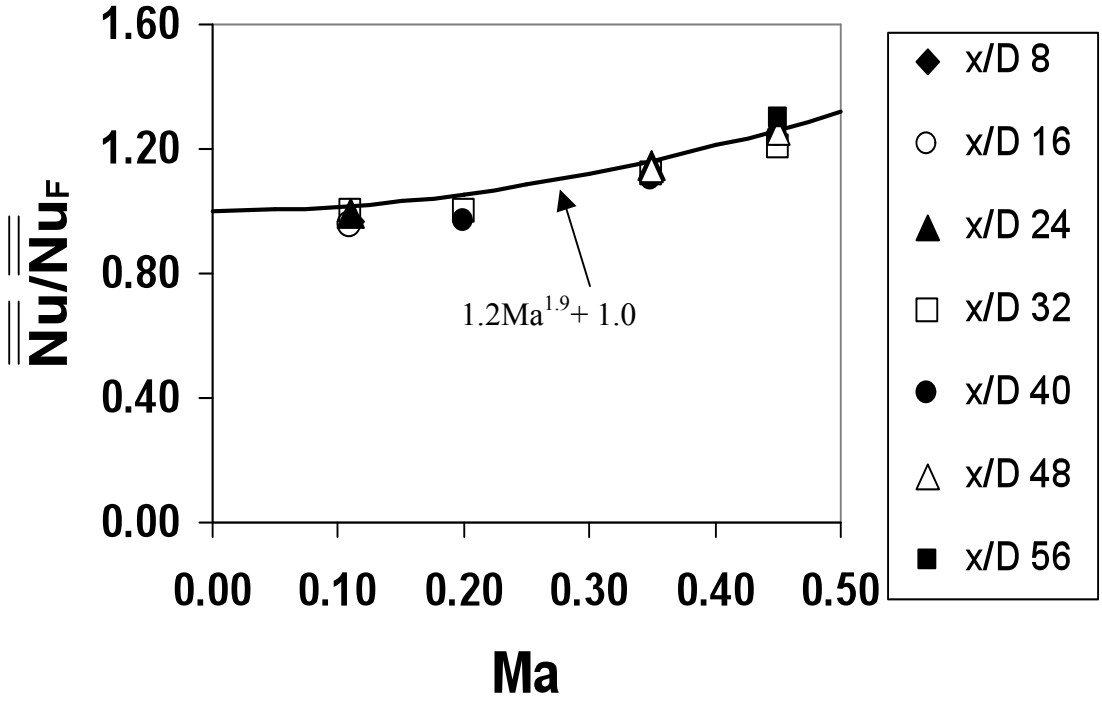

Figure 5.8. Nusselt number correlation with Mach number for hole spacing X/D = 8, Re_j = 30,000 and Ma values of 0.11, 0.20, 0.35, and 0.45.

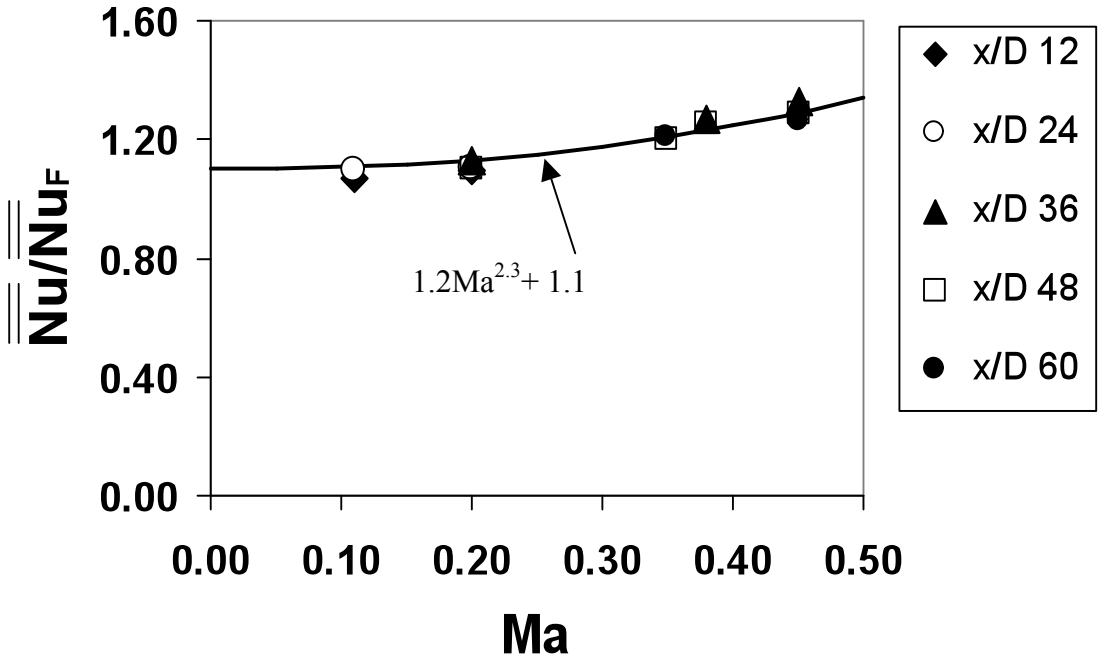

Figure 5.9. Nusselt number correlation with Mach number for hole spacing *X/D* = 12, Re_j = 30,000 and Ma values of 0.11, 0.20, 0.35, 0.38, and 0.45.

For $X/D = Y/D = 5$, the correlation equation which best represents these data is given by

$$\overline{\overline{Nu}}/\overline{\overline{Nu}}_F = 0.95 + 1.2Ma^{1.6} \tag{5.1}$$

For $X/D = Y/D = 8$, the associated correlation equation is given by

$$\overline{\overline{Nu}}/\overline{\overline{Nu}}_F = 1.0 + 1.2Ma^{1.9} \tag{5.2}$$

For $X/D = Y/D = 12$, the resulting correlation equation is given by

$$\overline{\overline{Nu}}/\overline{\overline{Nu}}_F = 1.1 + 1.2Ma^{2.3} \tag{5.3}$$

Figure 5.10 shows a comparison of the three trends predicted by these new correlations, clearly showing a strong dependence on Mach number which increases with decreasing hole spacing.

5.5 Summary and Conclusions

Both compressible and incompressible data are provided as the jet hole spacing is varied for Reynolds number equal to 30,000 and Mach number values ranging from 0.1 to 0.45. The spacings between holes in the streamwise direction X are then $5D$, $8D$ or $12D$, and the spanwise spacings between holes in a given streamwise row Y are also $5D$, $8D$ or $12D$. The thickness of each impingement plate is $1D$, and the spacing between the hole exit planes and the target plate is denoted Z and is equal to $3D$. These data are given for an array of impinging jets in the form of spatially-resolved local surface Nusselt numbers, line-averaged Nusselt numbers, and spatially-averaged Nusselt numbers.

For each of the jet spacings, local, line-averaged, and area-averaged data show strong Mach number dependence, provided the impingement jet Mach number is greater than about 0.2. Each jet produced using $X/D = Y/D = 12$ approximates the behaviour of an individual jet, whereas the influences of surrounding jets, including the

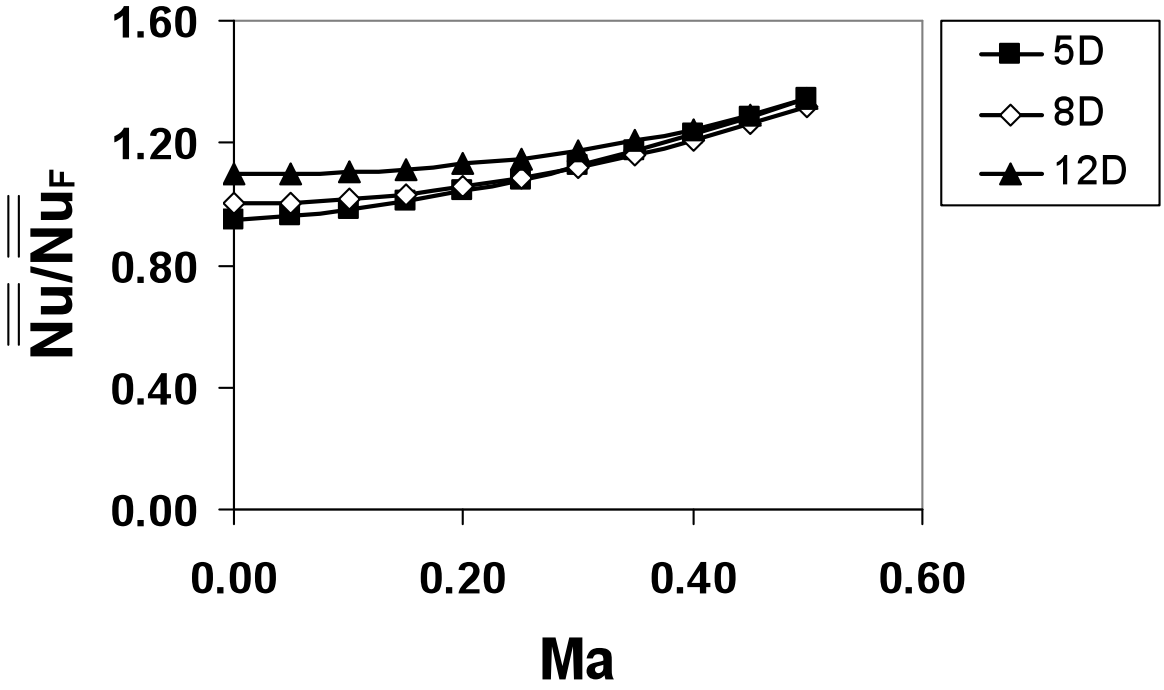

Figure 5.10. Comparison between Nusselt number correlations for hole spacings of 5, 8, and 12.

cumulative induced cross-flows and interactions of jet-induced vortex structures, alter the effectiveness of each individual jet when $X/D = Y/D = 8$. The interactions between adjacent jets are still stronger for $X/D = Y/D = 5$. Spatially-averaged Nusselt numbers for are generally higher at closer hole spacings than values for more sparse arrays when compared at the same streamwise location. The 12*D* jet spacing data show the least variation with x/D while the 5*D* jet spacing shows the most. Comparisons of periodic line-averaged Nusselt number data show that values decrease significantly at successive x/D locations for $X/D = Y/D = 5$, whereas $X/D = Y/D = 12$ data are approximately invariant with x/D. Regardless of the Reynolds number and the Mach number, the qualitative local Nusselt number distributions produced by different impingement jets are similar, with good periodic repeatability in the spanwise direction for each row of streamwise impact location.

Each of the three hole spacing configurations show strong dependence on Mach number, for Mach numbers greater than 0.2 as Reynolds number is held constant. Increasing the Mach number improves heat transfer for each geometry to differing degrees, with the greatest effect seen for the $X/D = Y/D = 5$ array.

Chapter 6

Experimental Facility and Measurement Techniques for the Film Cooling Study

6.1 Experimental Apparatus

The description of the film cooling experimental facility is presented in three sections. First the film cooing flow facility is presented, followed by a description of the test surfaces. Finally, the air pressure and temperature measurement techniques are explained. This facility is intended to model flow conditions found in combustor liners. The combustor section in fig. 1.4 has both a flat (minimal pressure gradient) and an inclined (strong pressure gradient) region. The focus on the present work is on the inclined region with limited data for a flat surface to provide comparison.

6.1.1 Film Cooling Facility

Schematic diagrams of the facility used for the film cooling study are presented in Figures 6.1 and 6.2. The facility consists of an inlet bellmouth, a variable contraction test section, a transition duct, and a centrifugal fan. Figure 6.1 shows the facility arrangement and airflow scheme. The pressure difference driving the freestream airflow is generated by a 415 V 3-phase Woodcock & Wilson 630 BFN single inlet centrifugal fan located downstream of the test section. The fan frequency is modulated by a 45 kW 2 pole ABB ACH550-01-096A-4+B056 Motor Drive. At the end of the inlet bellmouth contraction is an ultra-fine heater mesh powered by a 150 kW DC DRAKA Power Supply and a turbulence grid intended to generate flow mixing to insure the temperature increase from the heater mesh is uniform and increase the pressure drop in the freestream prior to the film-cooled surface. The heater mesh is used because it provides a near step change increase in free-stream temperature. After passing through the heater mesh, the bulk flow enters the working section where it experiences uniform acceleration as

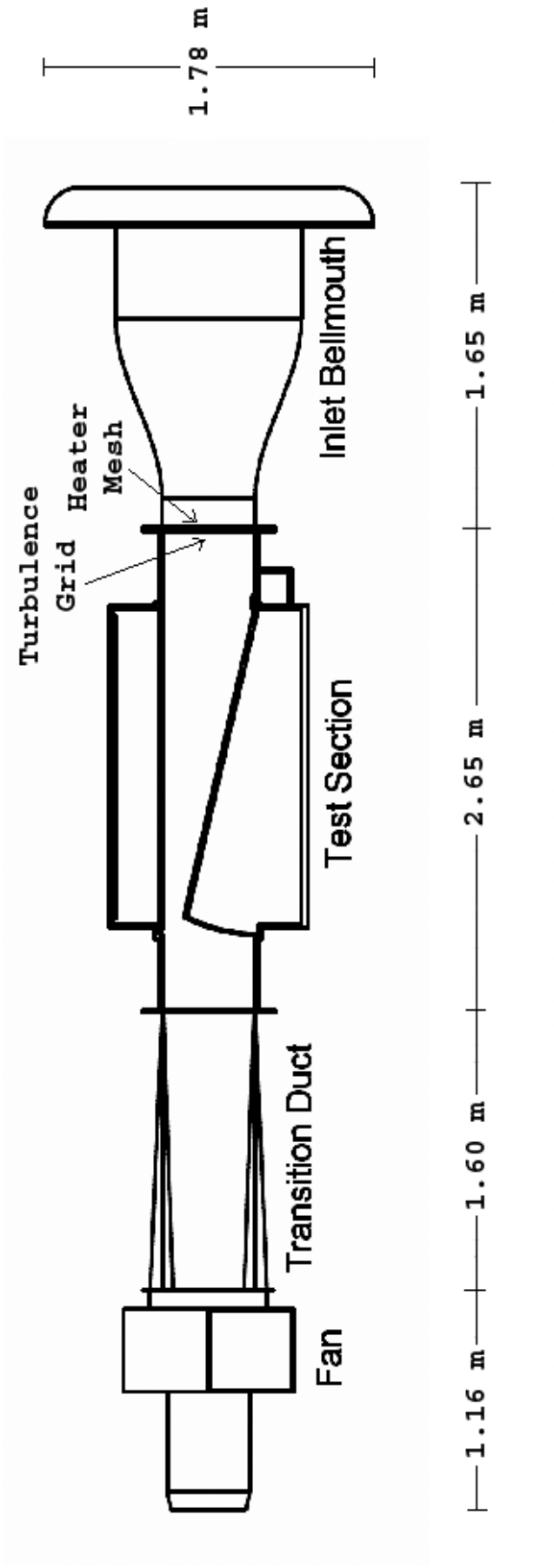

Figure 6.1. Overview of film cooling test facility.

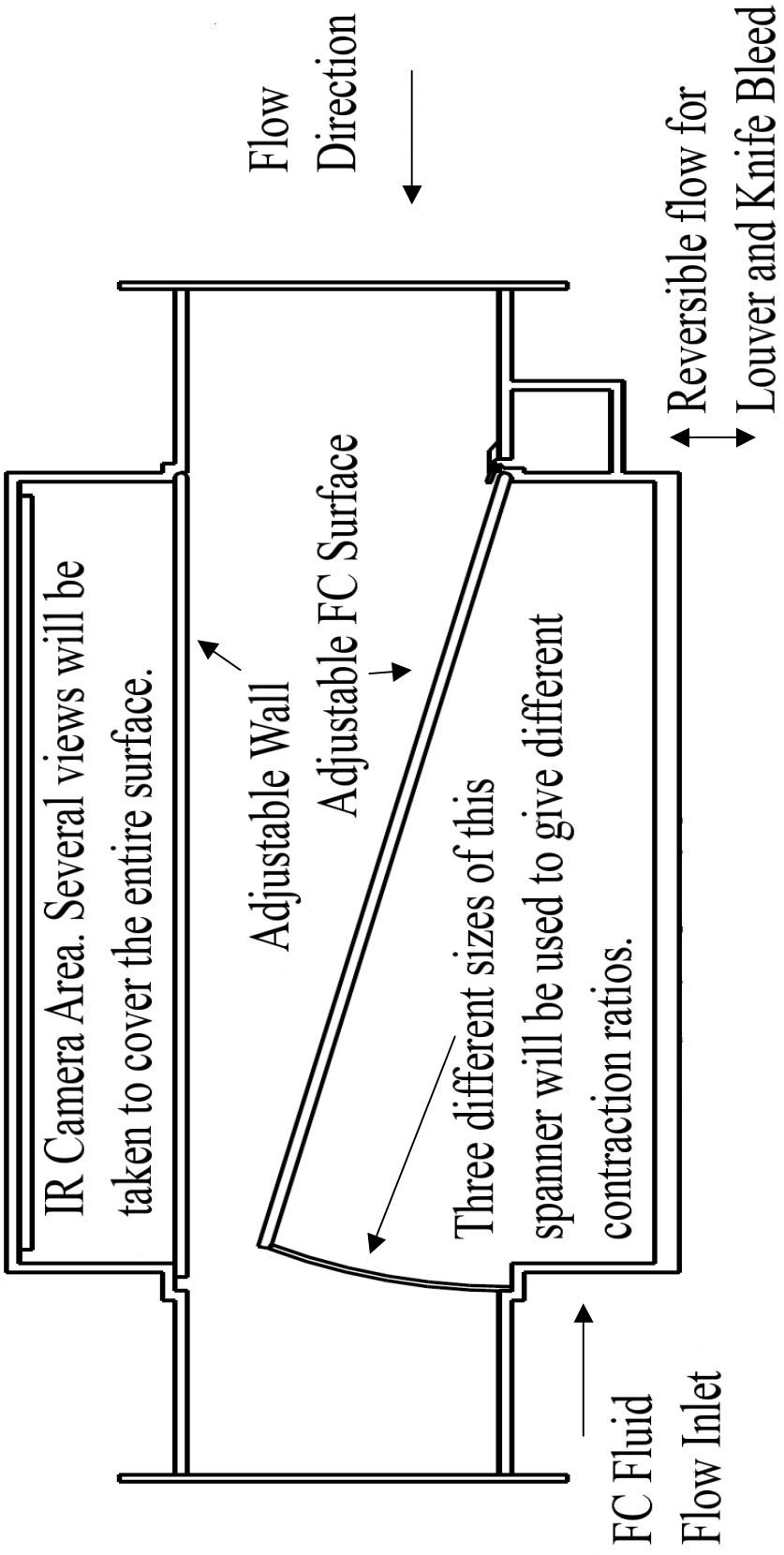

Figure 6.2. Film cooling test section.

it passes through the variable contraction. It then enters a transition duct and passes into the centrifugal fan. The film cooling flow is generated by the pressure difference between the atmospheric air and the air in the wind tunnel after the pressure drop across the heater mesh and the perforated plate and is supplemented by two Sodeca HEPT-35-2T/H 240 V single phase AC cased axial fans for the higher blowing ratio cases.

Figure 6.2 shows the inclined film cooled surface, the opposite wall which provides flow containment and window ports for the infrared camera, the film cooling flow inlet and the film cooling flow source chamber. The inclined film cooled surface consists of a frame and a test surface. The first row of film cooling holes is located 59.8 *mm* downstream of the contraction's beginning. The frame is made from 20mm Perspex. It is held in place by a pin hinge in the upstream end and is bolted to a Perspex spanner on the downstream end. It is surrounded by gasket material embedded in a machined groove. Additionally there are 8 L-shape brackets on the top and bottom of the frame that prevent flexing in the presence of a pressure difference between the bulk flow side and the film cooling flow source chamber. A flange with foam sealant and mounting clamps secure the test surface in place while guarding against leakage. The frame, test surface, Perspex spanner, and outside wall form the film cooling flow source chamber. This chamber is connected to the cased axial fan with five 8cm diameter flexible tubes. Because the volume and cross-section of the chamber are much larger than the area of the film cooling holes, the velocity in this part of the test section is approximately zero. This is an important approximation when determining the film cooling hole exit velocity using Bernoulli's equation. The wall opposite the film cooled surface has 8 ports spaced in such a way that the entire test surface can be imaged.

The film cooling flow is controlled by a valve that reduces the flow to the desired volume or for higher flow rates, the supplemental fans are used. For fine control at high flow rates, there is a potentiometer controlling the motor speed. Prior to the beginning of the film cooling surface there is a knife bleed to minimize boundary layer effects generated by the inlet bellmouth, heater mesh, and combustor liner test section entry length. The test

section is designed to include an optional louver which will be used for specified test cases in order to gauge its effect. Figure 6.3 presents a detail of the Louver. The first row of holes is 36.6 *mm* from the louver exit for each case presented. The suction for the knife bleed is provided by piping between the knife bleed and a position downstream of the contraction. This flow is measured by an ASME orifice plate and controlled by a valve. This can be reversed for the louver by opening the piping to lab air. Pitot static tubes placed at regular intervals with thermocouples along the top of the test section are used to verify the free-stream velocity, static pressure, free-stream temperature and density along the length of the film cooling surface.

6.1.2 Test Surfaces

The film cooling test surfaces are all made from 20mm Perspex with hole diameters of 7 mm. The usable test surfaces measure 400 mm by 1680 mm. The leading edge of the first row of film cooling holes is 60 mm from the leading edge of the test surface, giving 240 hole diameters of length before the end of the test surface. These dimensions were chosen because 7 mm is the smallest hole diameter that can be used without producing compressibility effects for at least one test case. The study employs five different test surfaces. The first has hole spacing X/D = 6, Y/D = 3 and hole angle inclined 20º to the surface, the second has X/D = 6, Y/D = 5 and hole angle 20º, the third has hole spacing X/D = 6, Y/D = 7 and hole angle 20º, the fourth has hole spacing X/D = 18, Y/D = 5 and hole angle 20º, and the fifth has hold spacing X/D = 6, Y/D = 5 and hole angle 30º.

6.1.3 Flow Measurement and Local Surface Temperatures

The pressure measurements are made using SensorTechincs® HCX series fully signal conditioned pressure transducers and fluid flow temperature measurements are made using chromel-alumel (K-type) thermocouples. Both types of sensors are connected to NI SCXI-1102B 32-Channel Amplifier Module though a NI SCXI-1303 Isothermal Terminal Block. The amplifier module is housed in a NI

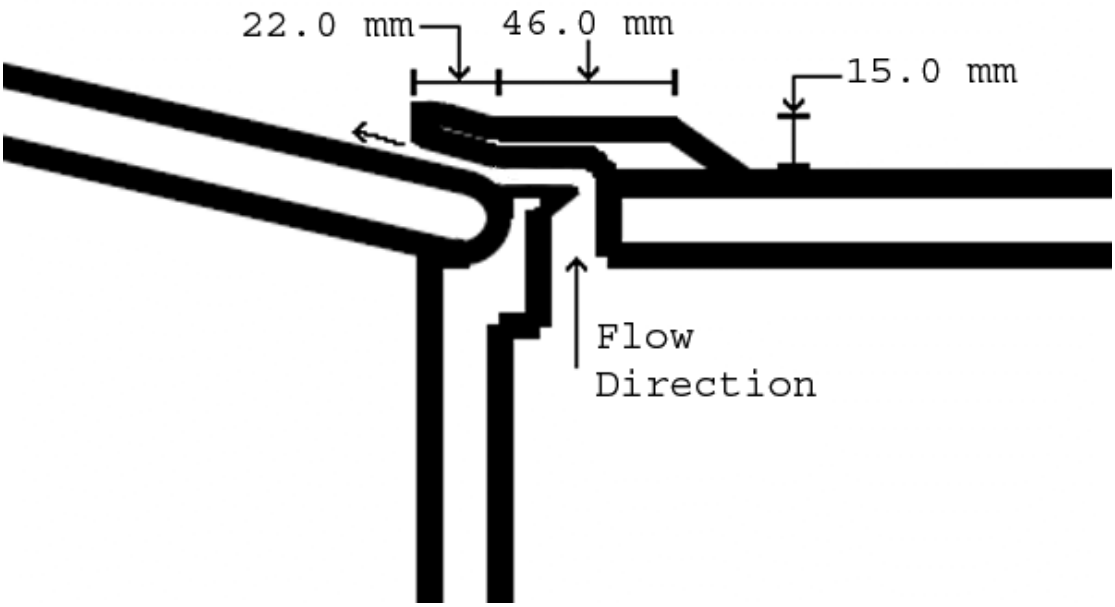

Figure 6.3. Detail of the contraction's beginning with the optional louver in place.

SCXI-1000 Chassis connected to a PC workstation through a NI PCI-6220 data acquisition board. Dynamic pressure is measured using pitot static tubes directly before the start of the contraction and near the end to find the freestream velocities at those points. The difference in static pressure is measured between the film cooling source chamber and four points along the contraction. Unlike the freestream velocity, this difference does not vary linearly with distance x along the contraction. Therefore a curve fitting routine is applied to the measured static pressure drops in order to find the static pressure difference between the film cooling source chamber and the freestream for each row of holes.

Surface temperature is determined through the use of a Flir ThermoVision® A20M far infrared camera (7.5 to 13 μm) which views the test surface through a zinc selenide window. The camera is calibrated through the use of K-type surface thermocouples in strategic locations. Thermocouple readings are recorded simultaneously with the acquisition of thermal contour images by the infrared camera at different surface temperatures. These images are converted into greyscale bitmaps and the thermocouple temperature and location information are used to develop a clear correlation between grayscale and temperature for the range of values used by the camera for a given experimental condition. When running a test, video is captured from the infrared camera at a rate of 15 frames per second. Each video frame from the infrared camera represents an array of wall temperatures at varying x and y locations for a give time t which is equal to the frame number multiplied by the sampling frequency.

6.2 Experimental Procedure

The present work focuses on providing local and spatially averaged effectiveness for a wide range of conditions. This data is produced using the impulse response method as developed at the University of Oxford.

6.2.1 Impulse Response Processing

The impulse response technique used to determine T_{aw} and h_f was originally developed to process signals from thin-film heat transfer gauges (Oldfield, 2008) and was first used by Guo et al. (2000) and Anthony et al. (1999, 2005). It was later used in conjunction with infrared thermography to measure heat transfer characteristics on turbine blade tips by O'Dowd et al. (2009). It is a computationally efficient method to reconstruct heat flux from discrete temperature samples taken at some sampling frequency f_s. It uses known pairs of exact solutions to generate an impulse response filter, which is used with MATLAB filter routines to convert temperature into heat flux using a Fast Fourier Transform and is fully described by Oldfield (2008).

6.2.2 Turbulence Intensity

Located 20 mm downstream from the heater mesh is a parallel array of round rods. This array serves two purposes. It mixes the bulk flow to eliminate or reduce any thermal non-uniformities following the heater mesh and generates a turbulent bulk flow field. The intensity of the turbulence downstream of the turbulence grid is determined according to:

$$Tu = C\left(\frac{x}{d}\right)^{-5/7} \tag{6.1}$$

where d is the diameter of the grid elements, x is the distance downstream from the grid, and C is a constant function of grid geometry and the drag force experienced by the individual grid elements. For the geometry in question, this value is 0.8 (Roach, 1986). At the beginning of the film cooling array, this equation gives a value of 8.5%.

6.2.3 Local and Line-Average Effectiveness

Film cooling effectiveness is a commonly used measure of dimensionless adiabatic wall temperature. It is defined as

$$\eta_{aw} = (T_{aw} - T_{\infty})/(T_c - T_{\infty}) \quad (6.2)$$

Effectiveness results facilitate the comparison between different cooling geometries and flow conditions because such results provide information on the coolant protection capabilities (Barigozzi et al.. 2006). The values of T_{aw} and h_f determined using impulse response processing, in conjunction with effectiveness measurements, provide the information necessary for fully describing film cooling heat transfer (Baldauf, 2001). Line-averaged effectiveness values are determined by averaging the effectiveness for a row of pixels at constant *x/D* for a range of *y/D* that includes one whole period in either direction from the line *y/D* = 0. For the plate with hole spacing *X/D* = 6, *Y/D* = 5, this range is from *y/D* = -5 to *y/D* = 5.

6.2.4 Blowing Ratio

The film fooling blowing ratio, B_R, is the ratio of film cooling mass flux to freesteam mass flux. It is represented mathematically as

$$B_R = \rho_c u_{fc} / \rho_{\infty} u_{\infty} \quad (6.3)$$

Both coolant density and freestream density are determined using measured values of temperature and pressure using the equation of state

$$P = \rho RT \quad (6.4)$$

and the ideal gas constant *R*, for air of 286.9 J/Kg•K, where the pressure, *P* and temperature, *T* are measured as described in section 6.1.1. The freestream velocity, u_{∞} is measured at two locations, immediately preceding and near the end of the contraction. This is done using pitot-static tubes and the relationship between dynamic pressure and velocity

$$u_{\infty} = \sqrt{2P_{dynamic} / \rho_{\infty}} \quad (6.5)$$

Film cooling velocity is determined using Bernoulli's equation for incompressible fluids, which for this case reduces to

$$P_c - P_\infty = \tfrac{1}{2}\rho u_{fc}^{\,2} \tag{6.6}$$

because of the zero approximation of the velocity in the film cooling flow source chamber. Additionally, a discharge coefficient of 0.72 is used when determining the film cooling velocity in this manner. This approach is used because the film cooling exit velocity changes significantly along the length of the film cooling surface due to the drop in static pressure along the contraction. This value of discharge coefficient was determined experimentally using a Davis 271 Turbo Meter which uses a freely turning turbine, whose rotation is sensed by an infrared beam, to measure flow velocity. Additionally this value shows good agreement with values reported by Gritsch et al. (2001) for round film cooling holes at an inclination angle of 30º. Rewriting Eq. 6.6 to include the discharge coefficient for the coolant exit velocity gives

$$u_{fc} = C_D \sqrt{2(P_c - P_\infty)/\rho_c} \tag{6.7}$$

The blowing ratio varies along the length of the film-cooled surface. The freestream mass flux increases as the density remains approximately constant and the velocity increases. The film cooling mass flux also increases along the contraction, because the static pressure difference driving the flow changes. The approximately linear increase in freestream velocity corresponds with an exponential drop in freestream static pressure. It is therefore sensible to calculate a blowing ratio for each row of holes.

6.2.5 Experimental Uncertainty Estimates

Uncertainty estimates are based on 95 percent confidence levels and are determined using methods described by Kline and McClintock (1953) and Moffat (1988). Uncertainty of temperatures measured with thermocouples is ±0.15°C. Spatial and temperature resolutions achieved with infrared imaging are about 0.1 mm to 0.2 mm, and 0.4°C, respectively. This magnitude of temperature resolution is due to

uncertainty in determining the exact locations of thermocouples with respect to pixel values used for the calibration of the infrared camera. The impulse response method has an uncertainty of ±5% for adiabatic wall temperatures and effectiveness.

6.2.6 Comparisons to Previous Work

Figure 6.4 compares local adiabatic effectiveness values at x/D = 1.25 for a single hole at BR = 0.5 for the configuration used in the present study with data from Ling et al. (2002) and Burd and Simon (1997). Both the present study and Ling et al. (2002), use film cooling hole axially aligned to the bulk flow and angled 20º to the cooled surface. Burd and Simon (1997) also use axially aligned holes, but theirs are inclined 35º to the surface. Good agreement is shown between the data of the present study and that of Ling et al. (2002). The data of Burd and Simon (1997) is somewhat lower than the other two values. This is typical when comparing a 35º hole with a 20º hole as effectiveness values decline more rapidly for a 35º injection hole.

Figure 6.5 shows additional comparison work done for high blowing ratio, full array film cooling cases. While the hole spacing is not the same for these cases, this comparison provides valuable information regarding the suitability of the new facility developed at the University of Oxford and the data reduction methods employed. The effectiveness data at hole spacings X/D = 8, Y/D = 4 and X/D = 5.67, Y/D = 5.67 is presented by Lin et al. (2003), the data at hole spacing X/D = 4.9, Y/D = 4.9 is presented by Scrittore et al. (2007) and the data at X/D = 6, Y/D = 5 was obtained using the new facility at the University of Oxford which was run without a flow contraction to better match the other investigations. The hole spacings investigated by Lin et al., which are similar to those of the present investigation, show good agreement with the data obtained at the University of Oxford. The data obtained by

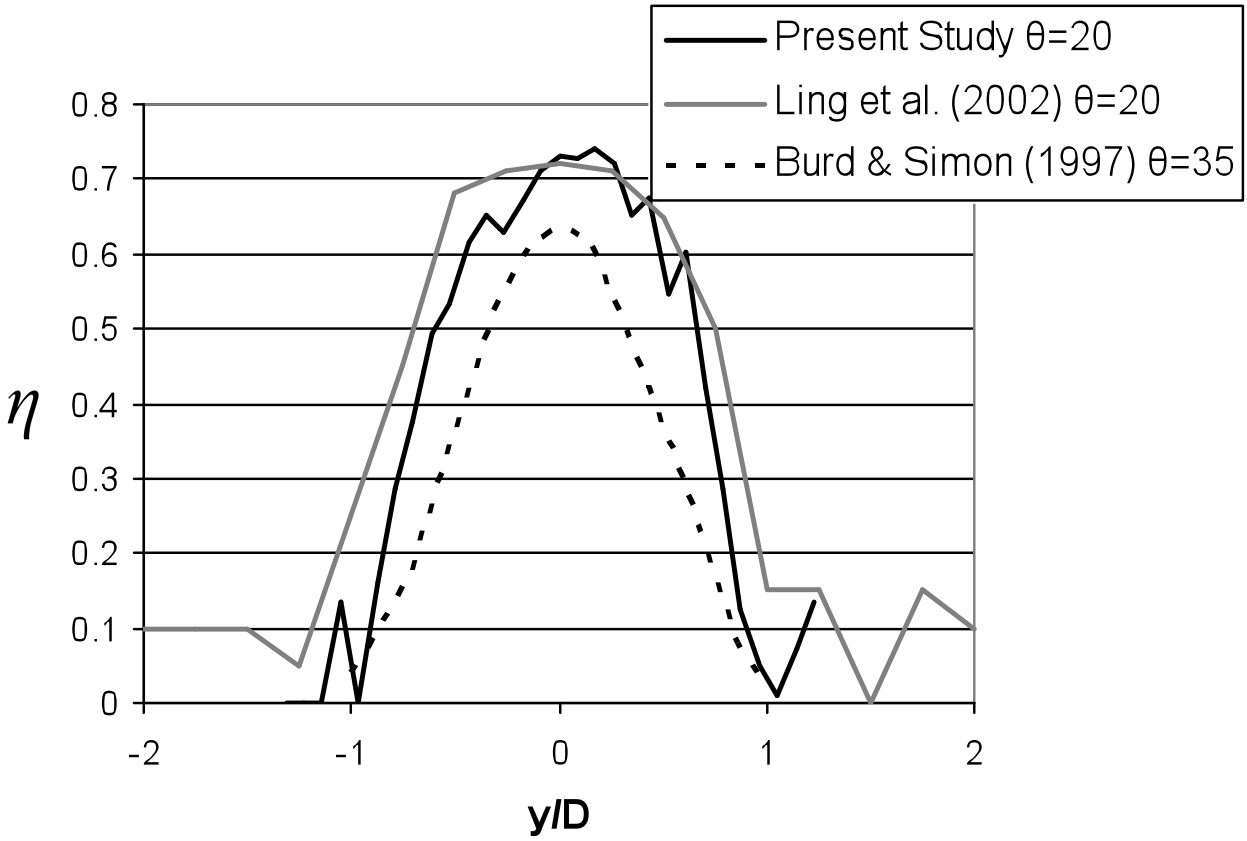

Figure 6.4. Local effectiveness comparison plot for a single film cooling hole at *BR* = 0.5 and *x/D* = 1.25.

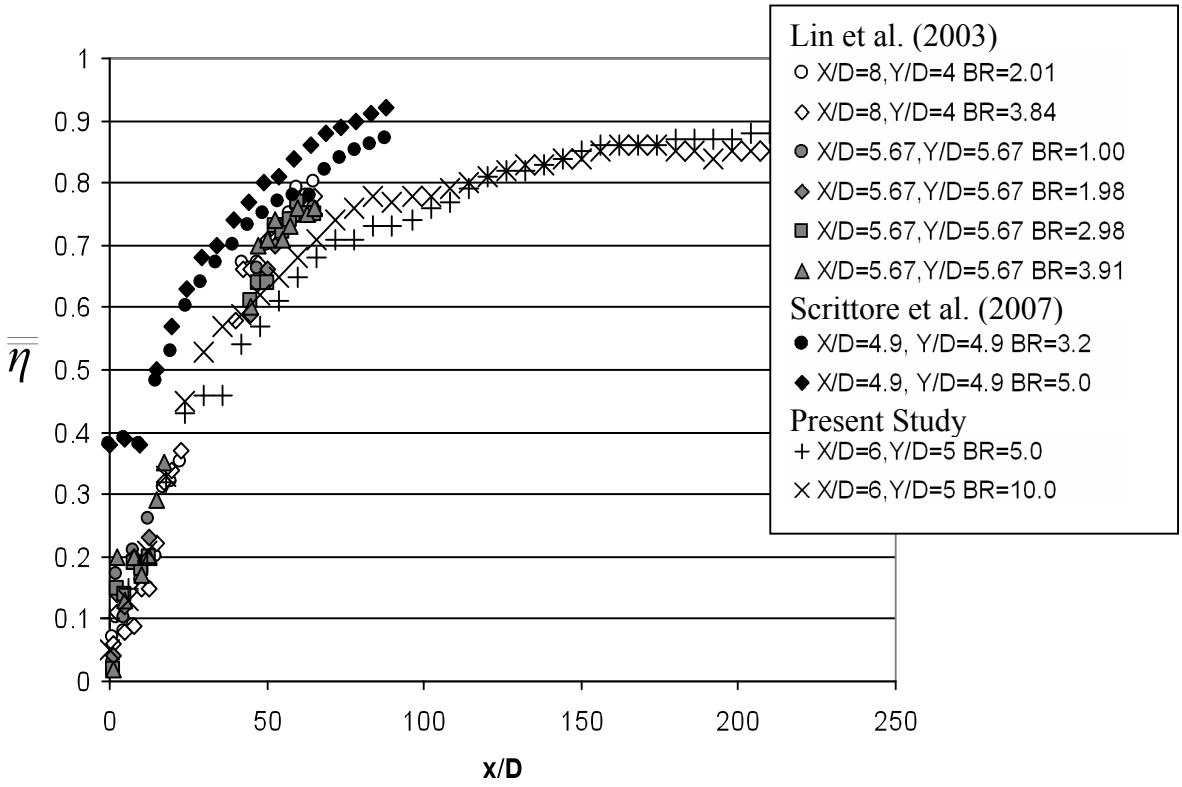

Figure 6.5. Spatially averaged effectiveness comparison plot.

Scrittore et al. are from a denser array and show the expected increase for such a configuration. However, there is still good qualitative agreement. For each of the cases in fig. 6.5, spatially averaged effectiveness increases with increasing *x/D*. This is caused by the contributions to the protective film made by subsequent rows of film cooling holes.

Chapter 7

Film Cooling in Gas Turbine Combustors

7.1 Overview

Data is obtained for each combination of blowing ratio, contraction ratio and hole spacing at two different film cooling Reynolds numbers and freestream temperatures. The Reynolds numbers used are Re_{fc} = 10,000 and Re_{fc} = 12,000 with a hole diameter of 7 mm and the freestream temperatures vary from 75ºC to 115ºC. These values were chosen to ensure the film cooling flow leaving the holes is turbulent and to generate density ratios in the range from 1.15 to 1.25.

Spatially averaged effectiveness values are plotted with one data point representing each row. These data points each represent effectiveness values averaged over an area from one half of the hole spacing value upstream to one half of the hole spacing value downstream of the row in question and two full hole spacings in the spanwise direction.

7.2 Blowing Ratios

Figure 7.1 shows each of the blowing ratio progressions examined in the present study. For each of the three blowing ratios examined, the increase in freestream velocity and corresponding increase in film cooling exit velocity causes decreasing blowing ratio with increasing *x/D*. From the 1st to the 39th row of holes this drop in blowing ratio ranges from 1.6% for the case *BR* = 2, *Cr* = 1 to 80% for the case *BR* = 10, *Cr* = 5. Specific data sets are reported in terms of blowing ratio, contraction ratio and hole spacing. For each case presented, the blowing ratio reported is the blowing ratio for the first row of holes only.

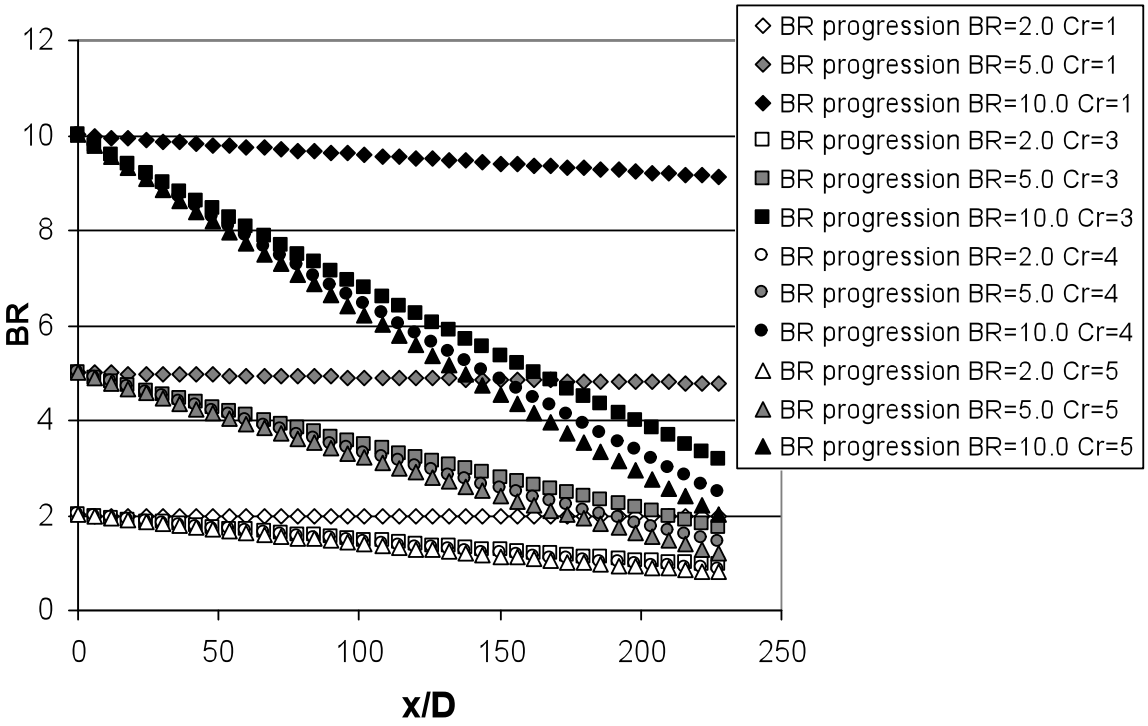

Figure 7.1. Blowing ratio progression with *x/D* for different contraction ratios, calculated on the basis of static pressure ratios.

7.3 Hole Spacing and Blowing Ratio Effects

Figures 7.2, 7.3, and 7.4 present spatially resolved effectiveness values for hole spacings of X/D = 6, Y/D = 3, X/D = 6, Y/D = 5, and X/D = 6, Y/D = 7 at blowing ratios of 2.0, 5.0, and 10.0 using a contraction ratio of 4. These conditions are representative of those used in modern gas turbine combustors ((Sasaki et al., 1979), (Leger et al., 2002), (Lin et al., 2003), (Scrittore et al., 2007). Careful examination of fig. 7.2 shows the development of a protective film between the second and third row of holes for each of the blowing ratios and a steady improvement in effectiveness until roughly the 12th row of holes (x/D=60) after which no visible improvement is made. It is noteworthy that the effectiveness is higher for the case BR = 5.0 than BR = 2.0, but that the values are approximately equal for BR = 5.0 and BR = 10.0.

Both figs. 7.3 and 7.4 demonstrate the same trend seen in fig. 7.2 of improving effectiveness with increasing x/D and a slight overall improvement for blowing ratios greater than 2.0. These figures also show that increasing the spacing between holes delays the generation of the protective film and decreasing the improvement rate of effectiveness with increasing x/D. Additionally, improvement does not appear to stop by the 12th row of holes as in the X/D = 6, Y/D = 3 case, but continues to improve throughout the visual data, around x/D = 95. For the cases BR = 5.0 and BR = 10.0 there are areas of higher effectiveness around the first row of holes. This is unexpected because at that point there is no protective film generated from the film cooling holes. This inconsistency is caused by a combination of high turbulence effects generated by the penetration of the first row of jets into the freestream and minor non-uniformities in heating the bulk flow at the lower freestream velocities

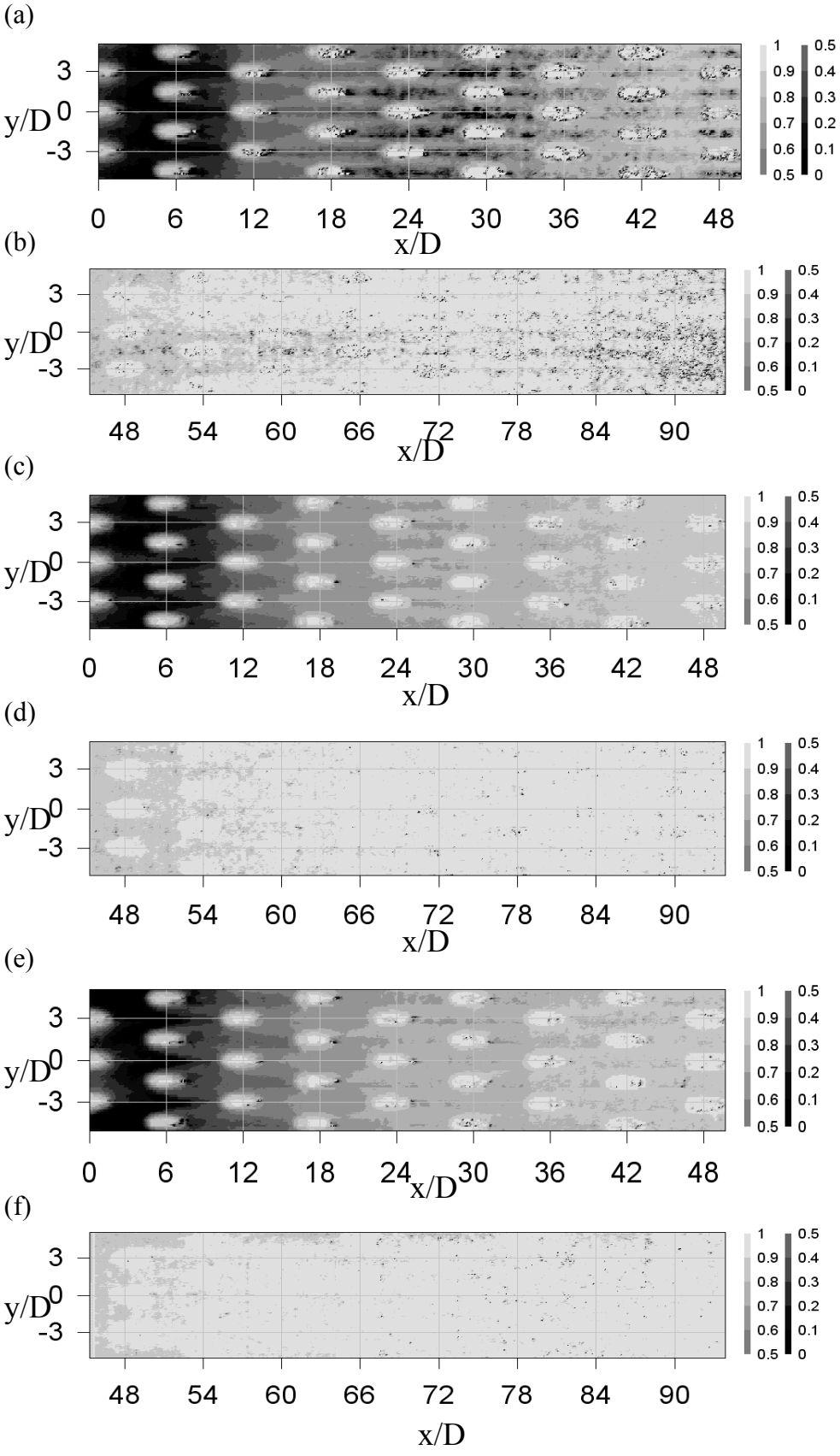

Figure 7.2. Spatially resolved effectiveness at blowing ratios for hole spacing $X/D = 6$, $Y/D = 3$, $Cr = 4$, and (a) $BR = 2.0$, x/D from 0 to 50, (b) $BR = 2.0$, x/D from 46 to 95, (c) $BR = 5.0$, x/D from 0 to 50, (d) $BR = 5.0$, x/D from 46 to 95, (e) $BR = 10.0$, x/D from 0 to 50, and (f) $BR = 10.0$, x/D from 46 to 95.

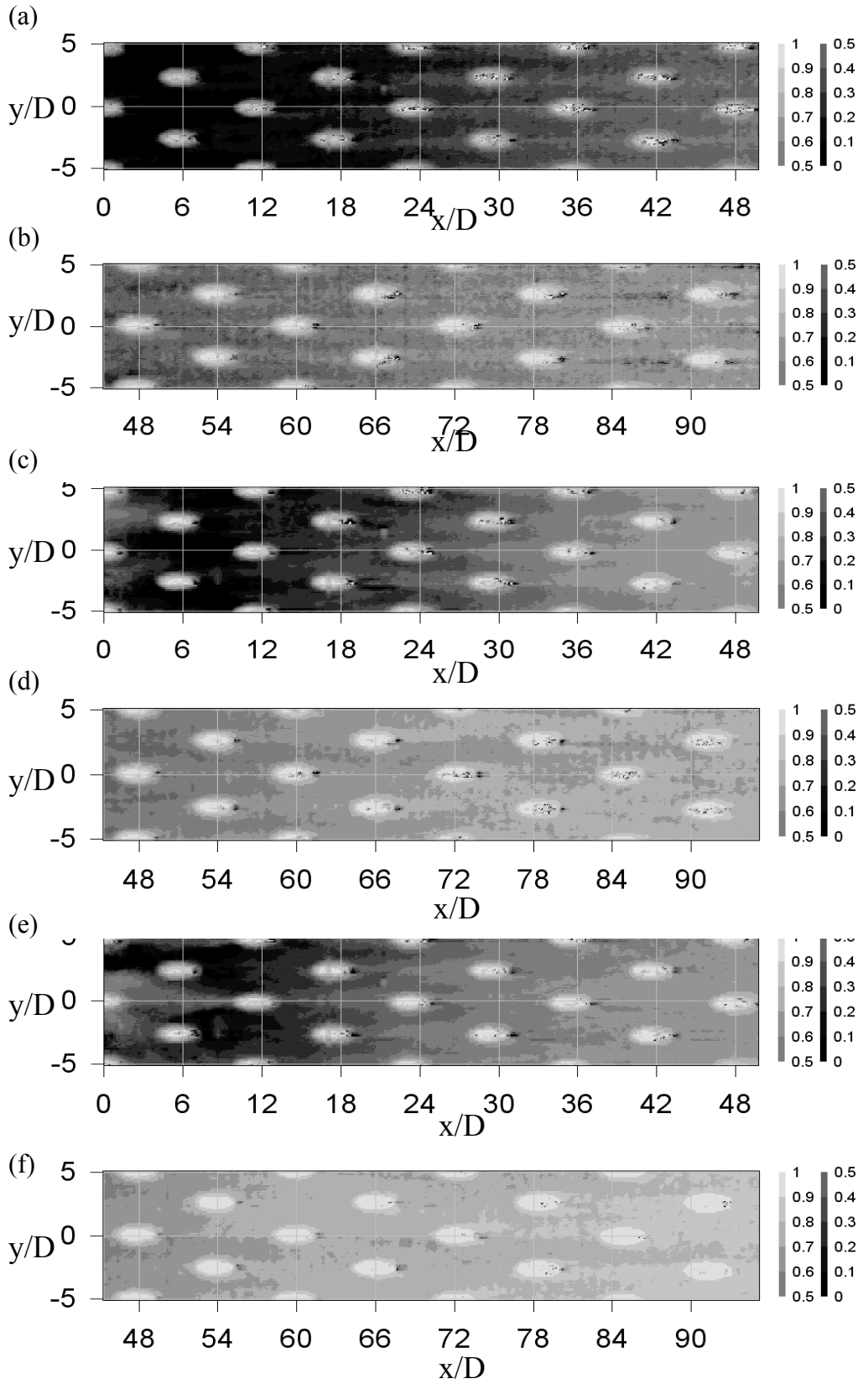

Figure 7.3. Spatially resolved effectiveness at blowing ratios for hole spacing *X/D* = 6, *Y/D* = 5, *Cr* = 4, and (a) *BR* = 2.0, *x/D* from 0 to 50, (b) *BR* = 2.0, *x/D* from 46 to 95, (c) *BR* = 5.0, *x/D* from 0 to 50, (d) *BR* = 5.0, *x/D* from 46 to 95, (e) *BR* = 10.0, *x/D* from 0 to 50, and (f) *BR* = 10.0, *x/D* from 46 to 95.

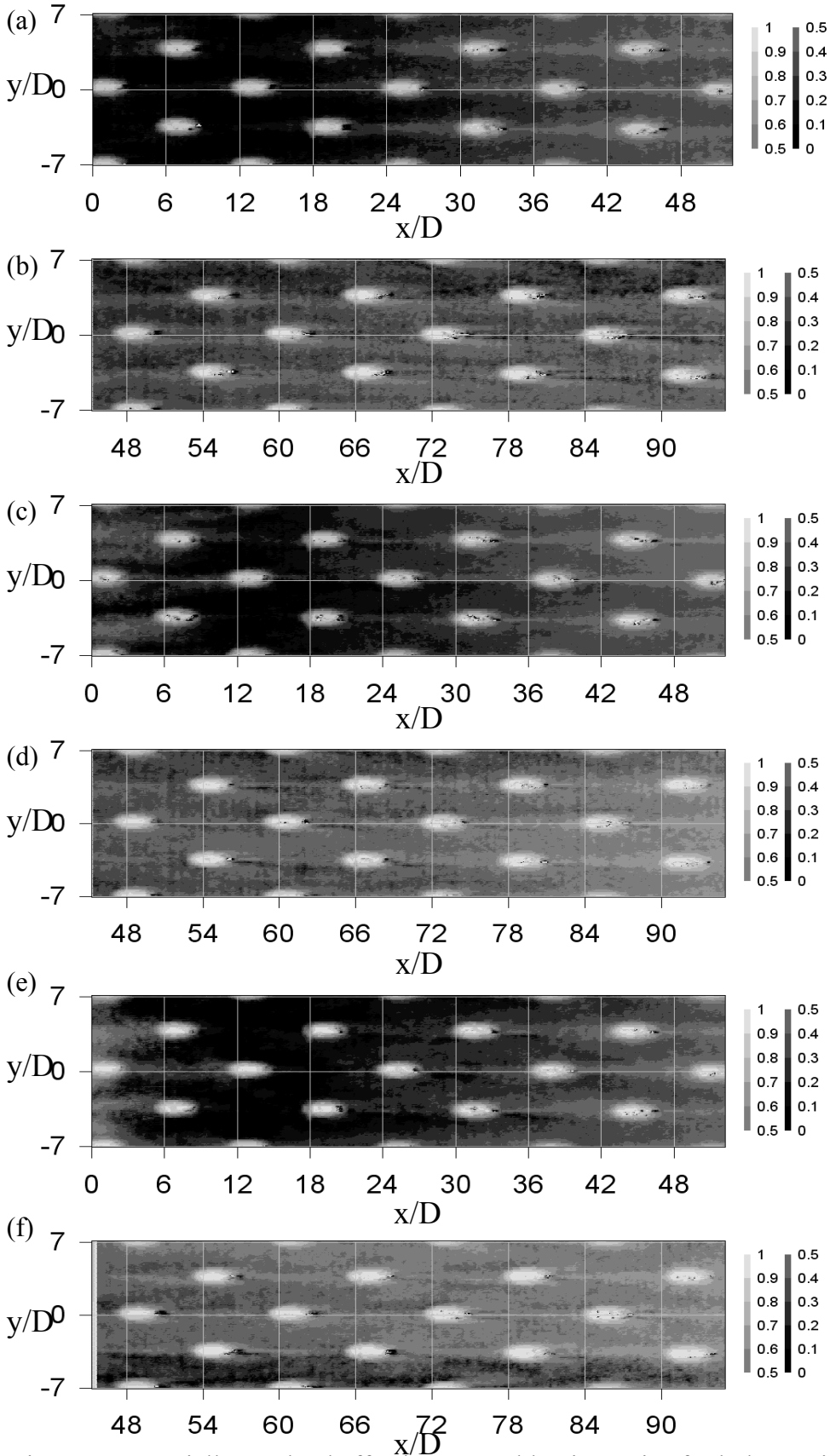

Figure 7.4. Spatially resolved effectiveness at blowing ratios for hole spacing X/D = 6, Y/D = 7, Cr = 4, and (a) BR = 2.0, x/D from 0 to 51, (b) BR = 2.0, x/D from 46 to 94, (c) BR = 5.0, x/D from 0 to 51, (d) BR = 5.0, x/D from 46 to 94, (e) BR = 10.0, x/D from 0 to 51, and (f) BR = 10.0, x/D from 46 to 94.

present in the facility when running tests at blowing ratios greater than 2.0. This effect is no longer present by the third row of holes for any of the conditions investigated in the present study.

Figures 7.5, 7.6, and 7.7 present spatially averaged effectiveness as it varies with streamwise position x/D for hole spacings X/D = 6, Y/D = 3; X/D = 6, Y/D = 7; X/D = 6, Y/D = 7 and blowing ratios 2.0, 5.0, and 10.0 respectively. These figures quantify the observable changes in effectiveness with decreasing hole spacing in figs. 7.2, 7.3, and 7.4. For each of the blowing ratios presented in figs. 7.5, 7.6, and 7.7 there exists a strong correlation between decreasing hole spacing and increasing effectiveness.

Figures 7.8, 7.9, and 7.10 also present spatially averaged data for cases previously examined in figs. 7.2, 7.3, and 7.4. This time however, the comparisons are for varying blowing ratio at different hole spacings. These data confirm the previously observation that there is a slight improvement in effectiveness when the blowing ratio is increased from 2.0 to 5.0 but there is no further improvement when the blowing ratio is increased to 10.0. This indicates that shortly after the blowing ratio increases above 2.0, the surface reaches an overcooled state and no further improvement is possible by increasing the coolant mass flow rate. This strong dependence on hole spacing and negligible dependence on the blowing ratio for dense film cooling arrays agrees with the findings of Lin et al. (2003) and Scrittore et al. (2007) who conclude that blowing ratio has a negligible affect on effectiveness for film cooling arrays with concurrent coolant injection.

7.4 Varying Contraction Effects

Figure 7.11 provides a comparison between 11 different flow conditions for a test surface with hole spacing X/D = 6, Y/D = 5. These conditions are obtained by

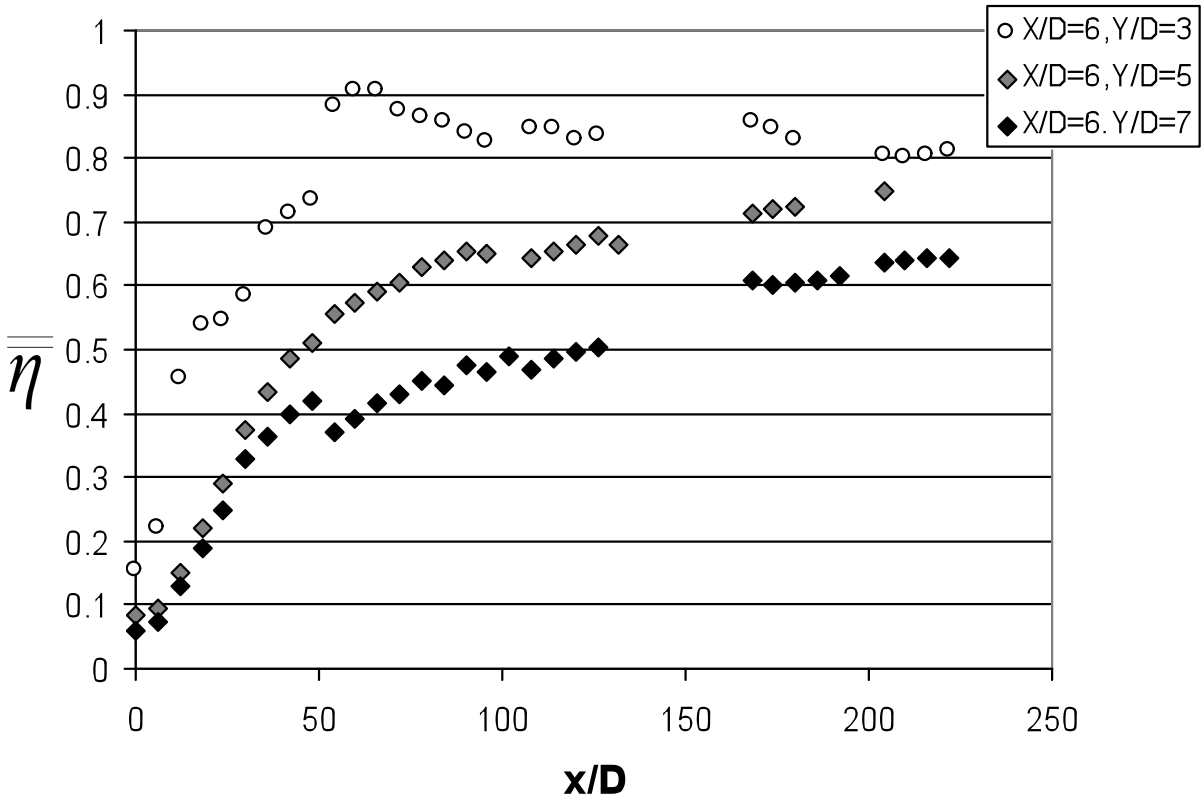

Figure 7.5. Variations of spatially averaged effectiveness at different hole spacings for $BR = 2.0$.

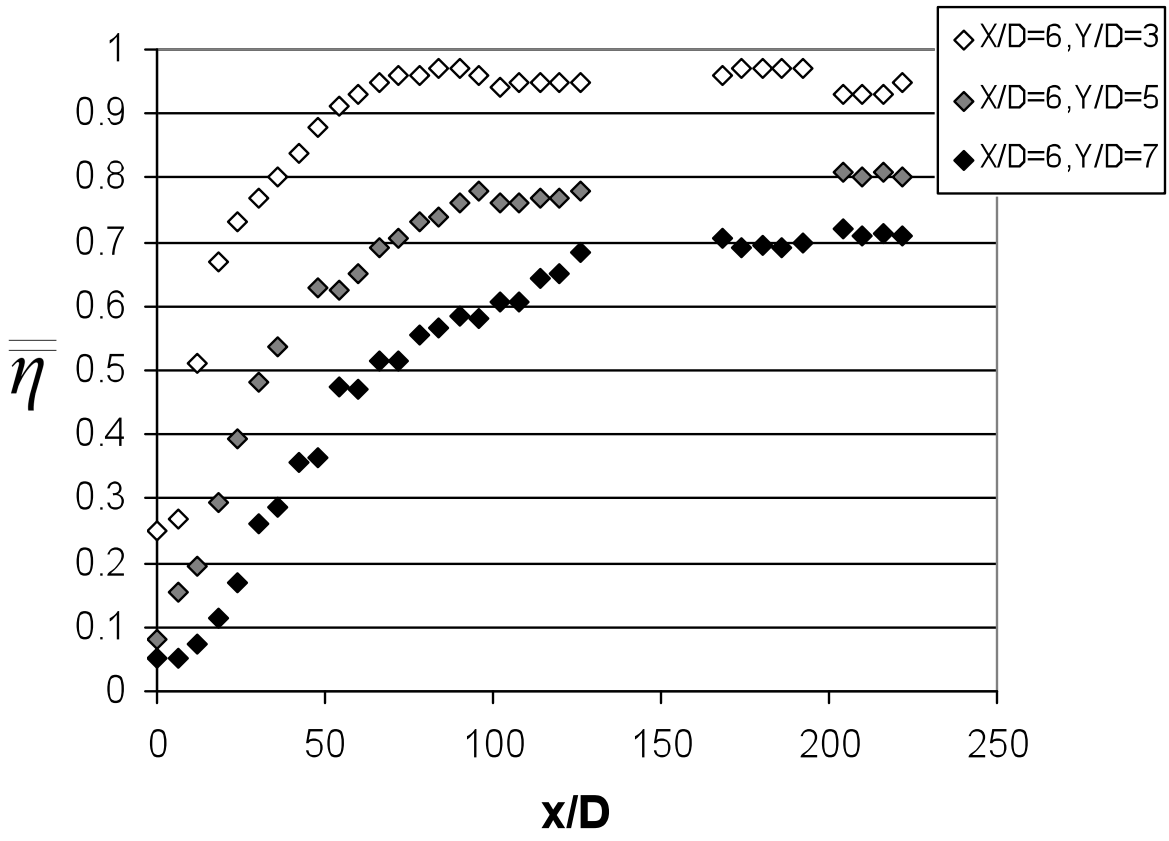

Figure 7.6. Variations of spatially averaged effectiveness at different hole spacings for $BR = 5.0$.

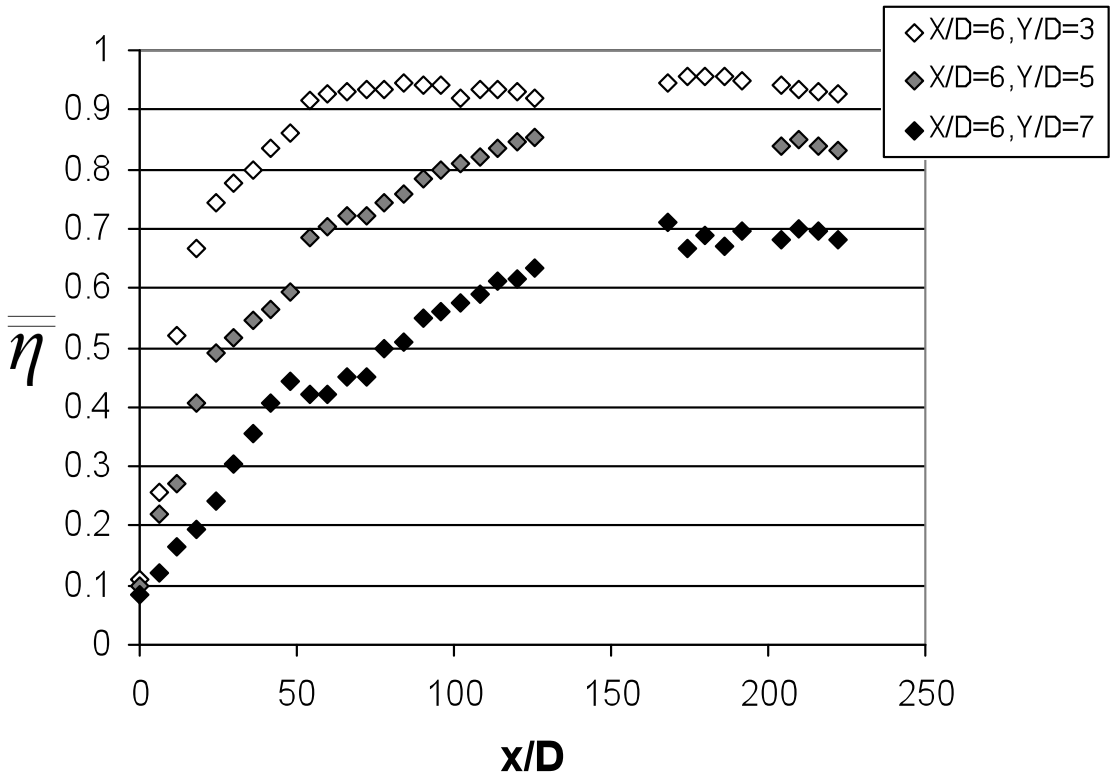

Figure 7.7. Variations of spatially averaged effectiveness at different hole spacings for $BR = 10.0$.

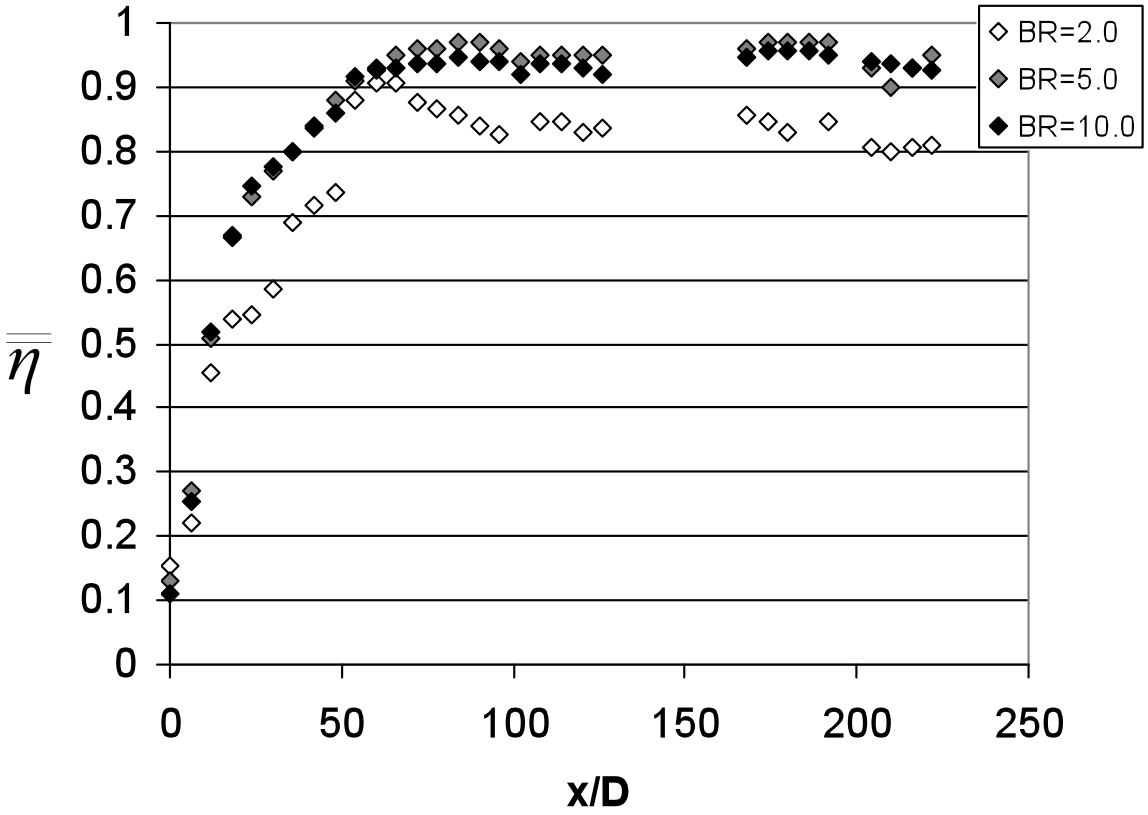

Figure 7.8. Comparison of spatially averaged effectiveness at different blowing ratios for hole spacing $X/D = 6$, $Y/D = 3$.

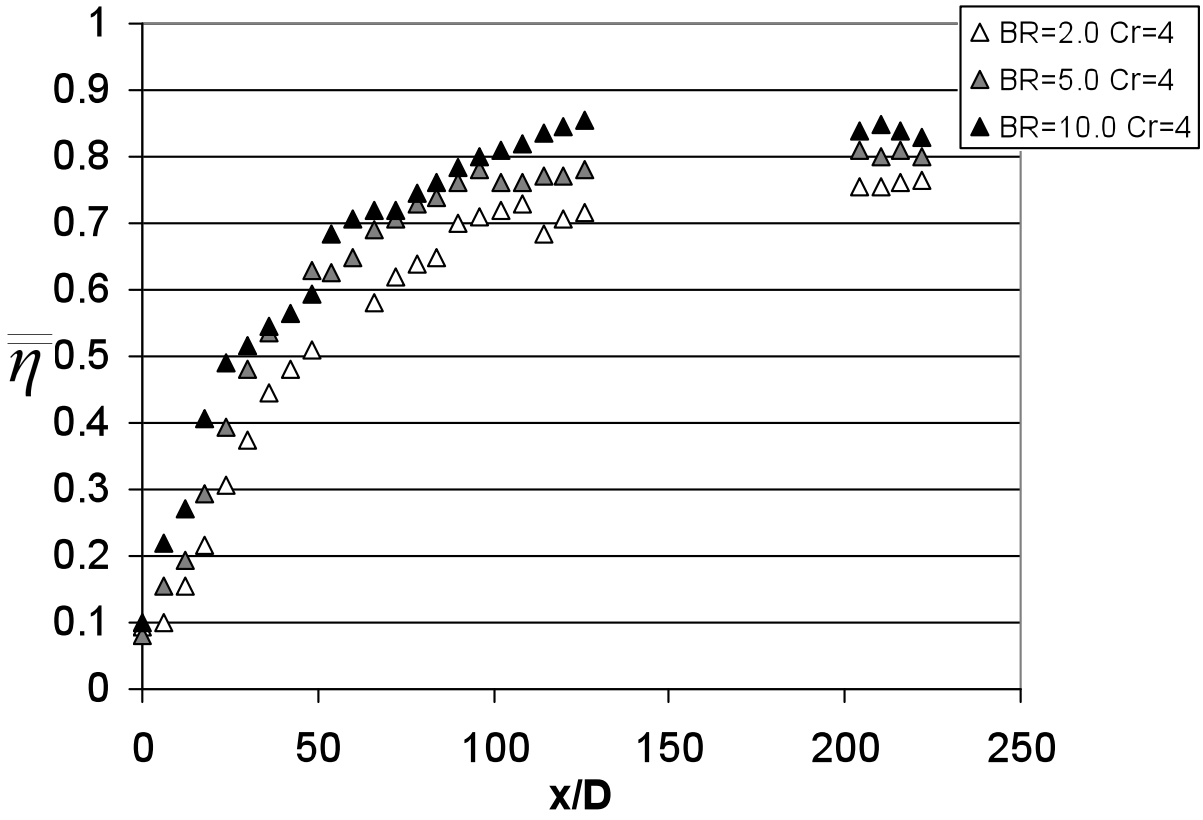

Figure 7.9. Comparison of spatially averaged effectiveness at different blowing ratios for hole spacing $X/D = 6$, $Y/D = 5$.

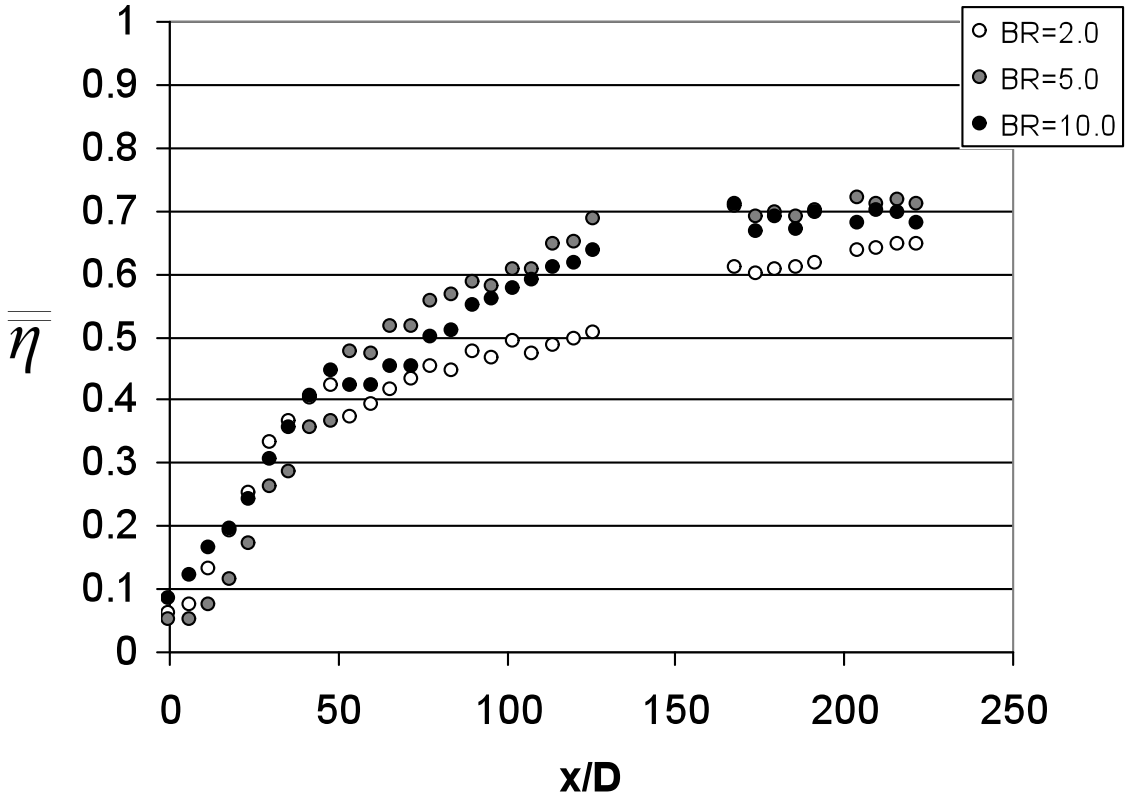

Figure 7.10. Comparison of spatially averaged effectiveness at different blowing ratios for hole spacing $X/D = 6$, $Y/D = 7$.

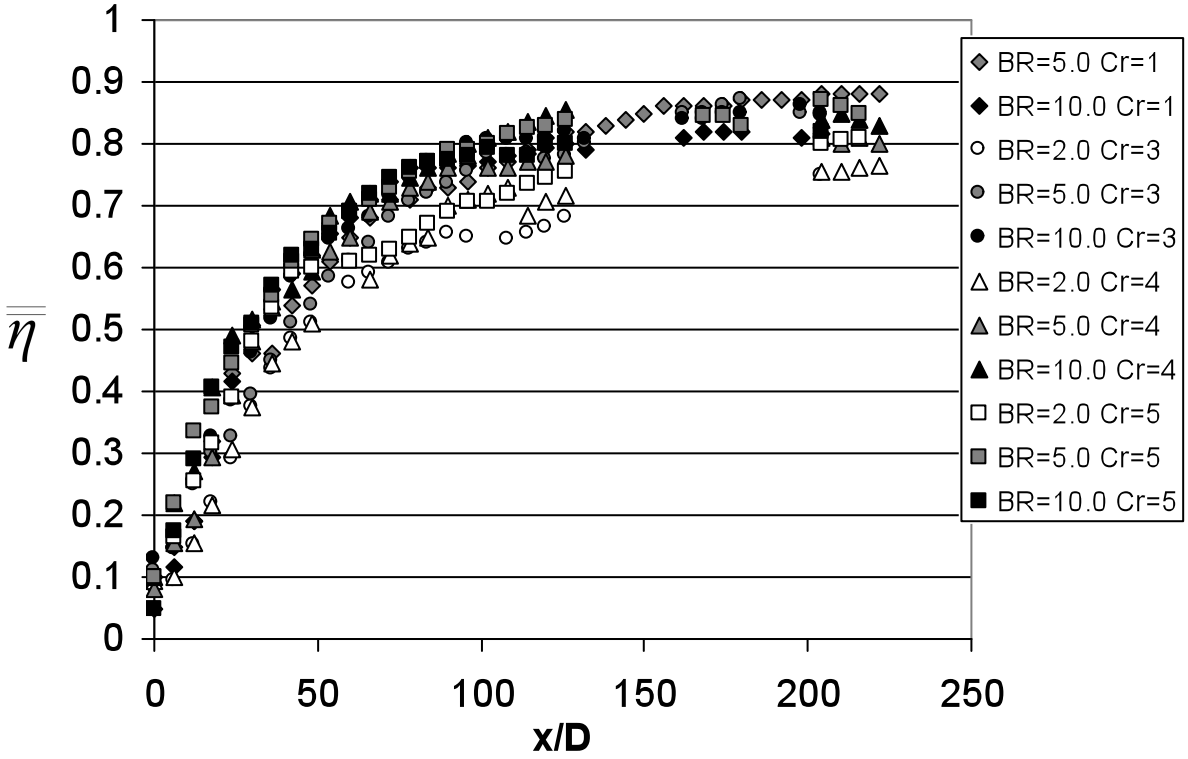

Figure 7.11. Comparison of spatially averaged effectiveness values for *X/D* = 6, *Y/D* = 5, blowing ratios 2.0, 5.0, and 10.0, and contraction ratios 1, 3, 4, and 5.

varying the blowing ratio and the contraction ratio. The figure shows that for each of the conditions examined, not only does varying the blowing ratio have negligible effect on effectiveness, but changes in contraction ratio also have no noticeable effect. As illustrated in fig. 7.1, the blowing ratio changes dramatically along the length of the test surface at different contraction ratios. This change in blowing ratio is the primary flow field variation associated with changing contraction ratio and because previously presented data already established that blowing ratio does not significantly affect effectiveness for dense film cooling arrays it is not surprising that the changes in blowing ratio associated with a changing contraction ratio also have no noticeable effect.

To better visualize the effect of varying blowing ratio and contraction ratio, data were collected for a relatively sparse array of X/D = 18, Y/D = 5. This data is also intended to determine if the favourable pressure gradient associated with a contraction has a positive affect on film cooling. Figures 7.12 and 7.13 present spatially resolved effectiveness values for X/D = 18, Y/D = 5, BR = 2.0, 5.0, and 10.0 at contraction ratios of 1.0 and 4.0 respectively. Figure 7.12 is highly reminiscent of fig. 7.3 which presents data for X/D = 6, Y/D = 5 and Cr = 4. In both cases a protective film forms at about the third row of holes and is followed by an increase in effectiveness with increasing x/D, there is a slight improvement from BR = 2.0 to BR = 5.0 and negligible change from BR = 5.0 to BR = 10.0, and both cases have unexpected areas of higher effectiveness around the first row or two of holes caused by a combination of high turbulence effects generated by the penetration of the first row of jets into the freestream and minor non-uniformities in heating the bulk flow.

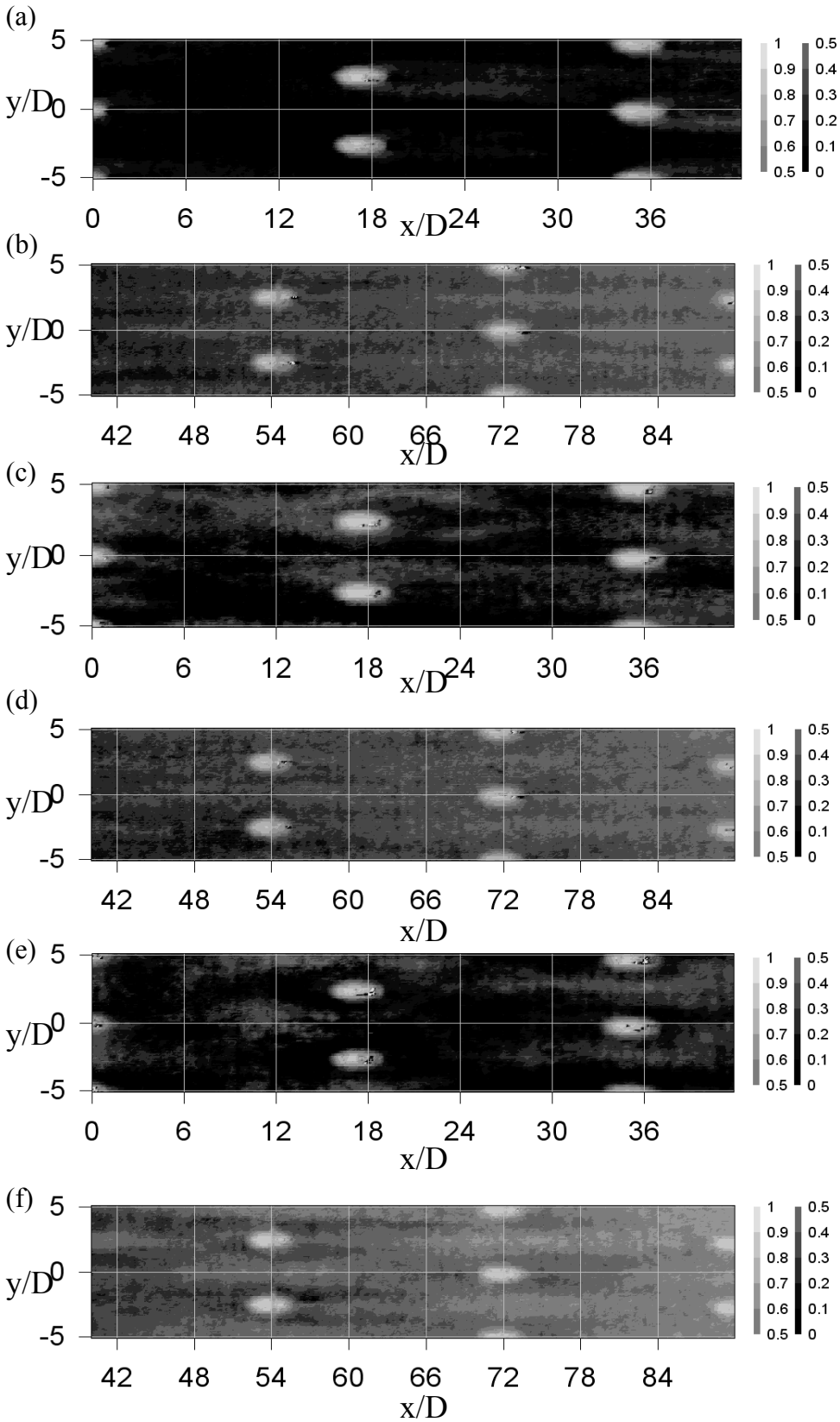

Figure 7.12. Spatially resolved effectiveness at different blowing ratios for hole spacing *X/D* = 18, *Y/D* = 5 and (a) *BR* = 2.0, *Cr* = 1, *x/D* from 0 to 41 (b) *BR* = 2.0, *Cr* = 1, *x/D* from 40 to 89 (c) *BR* = 5.0, *Cr* = 1, *x/D* from 0 to 41 (d) *BR* = 5.0, *Cr* = 1, *x/D* from 40 to 89 (e) *BR* = 10.0, *Cr* = 1, *x/D* from 0 to 41 (f) *BR* = 10.0, *Cr* = 1, *x/D* from 40 to 89.

Figure 7.13 shows results significantly dissimilar to those presented in fig. 7.12. The effectiveness at values of *x/D* greater than about 60 is lower for data sets *BR* = 2.0 and *BR* = 5.0 at *Cr* = 4 when compared to the same conditions at *Cr* = 1. This difference is not present for the case *BR* = 10.0. This decrease is due to the drop in blowing ratio with increasing values of *x/D*. For the case of the sparse array, when *Cr* = 1 the data posses the same overcooled characteristics present in the dense arrays. However, when the contraction ratio is 4, there is insufficient coolant to generate this overcooled condition. This finding is significant. As indicated by Ling et al.(2002), designers are interested in lean burning combustors with reduced coolant flow. Traditionally combustor liners are overcooled due to the high pressure ratios required by the injector and the dense arrays required to minimise thermal gradients. However innovative cooling schemes such as multi-layer liners make lower blowing ratios and more appropriate coolant flow rates possible. The affects associated with a contraction cause a significant change in cooling performance for conditions that are not overcooled. It is therefore essential that designers of leaner systems take these conditions into account to ensure proper cooling.

Figures 7.14 and 7.15 present spatially averaged data for the conditions covered in figs. 7.12 and 7.13. Figure 7.14 confirms the observation that for *Cr* = 1, hole spacing *X/D* = 18, *Y/D* = 5, and blowing ratios of 2.0, 5.0 and 10.0 the surface is overcooled. Figure 7.15 shows strong dependence of effectiveness on blowing ratio for hole spacing *X/D* = 18, *Y/D* = 5. This is the only condition presented thus far where contraction ratio has an observable effect on effectiveness measurements.

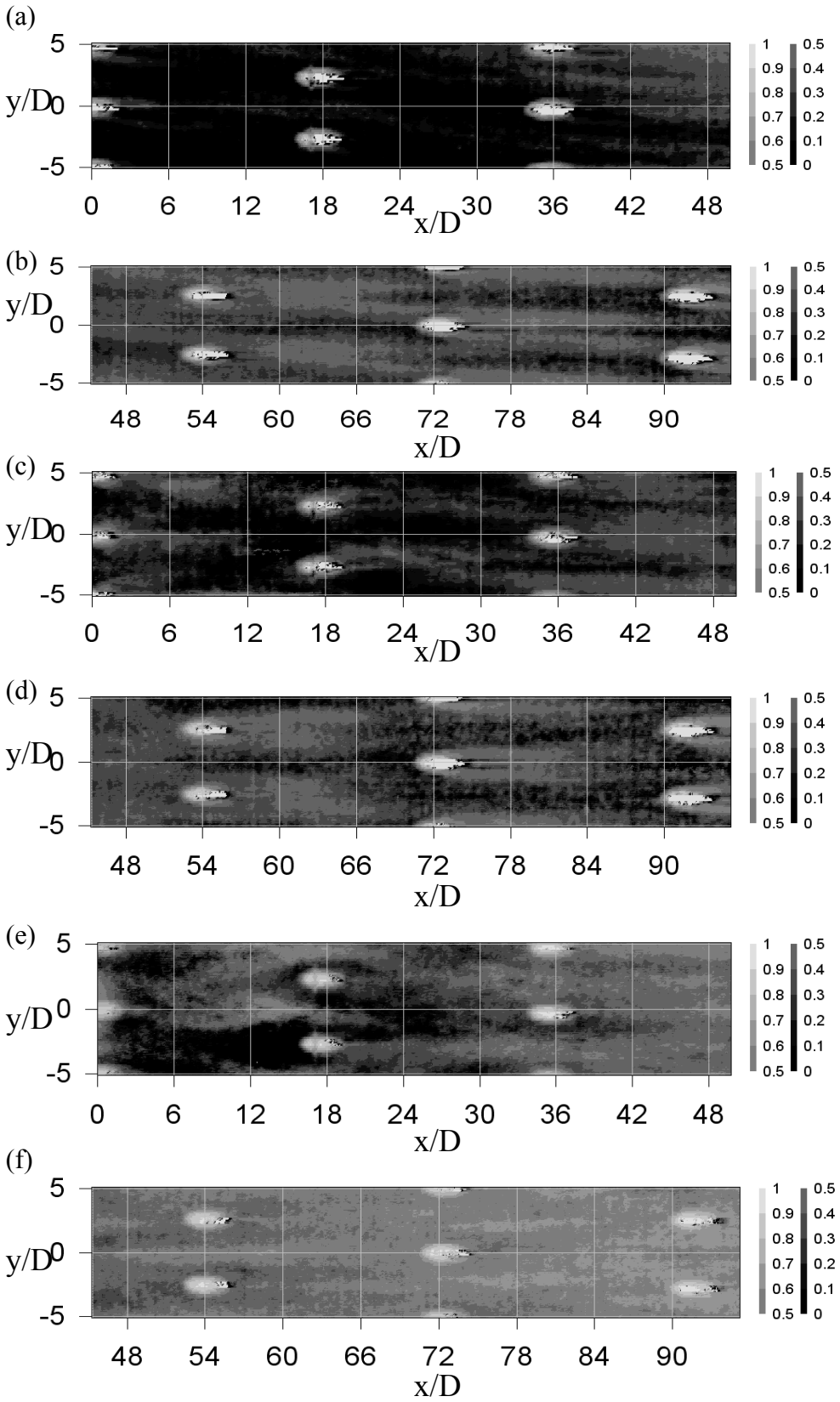

Figure 7.13. Spatially resolved effectiveness at different blowing ratios for hole spacing *X/D* = 18, *Y/D* = 5 and (a) *BR* = 2.0, *Cr* = 4, *x/D* from 0 to 50 (b) *BR* = 2.0, *Cr* = 4, *x/D* from 45 to 95 (c) *BR* = 5.0, *Cr* = 4, *x/D* from 0 to 50 (d) *BR* = 5.0, *Cr* = 4, *x/D* from 45 to 95 (e) *BR* = 10.0, *Cr* = 4, *x/D* from 0 to 50 and (f) *BR* = 10.0, *Cr* = 4, *x/D* from 45 to 95.

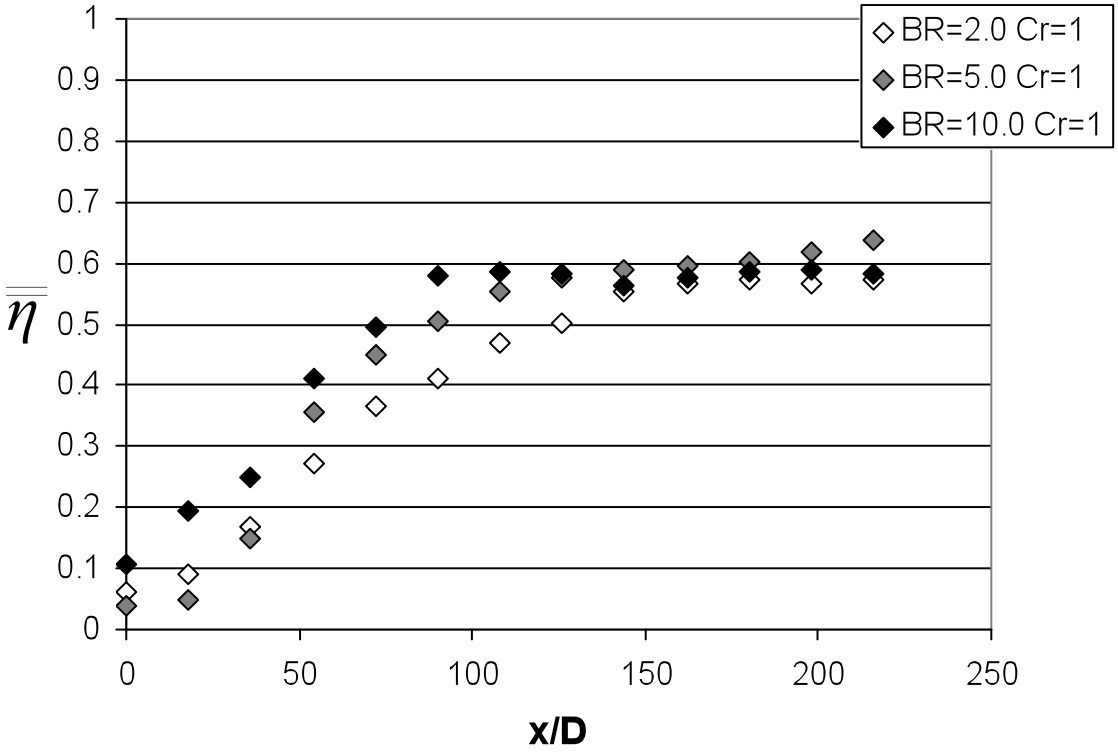

Figure 7.14. Spatially averaged effectiveness for *X/D* = 18, *Y/D* = 5, blowing ratios 2.0, 5.0, and 10.0, and a contraction ratio of 1.

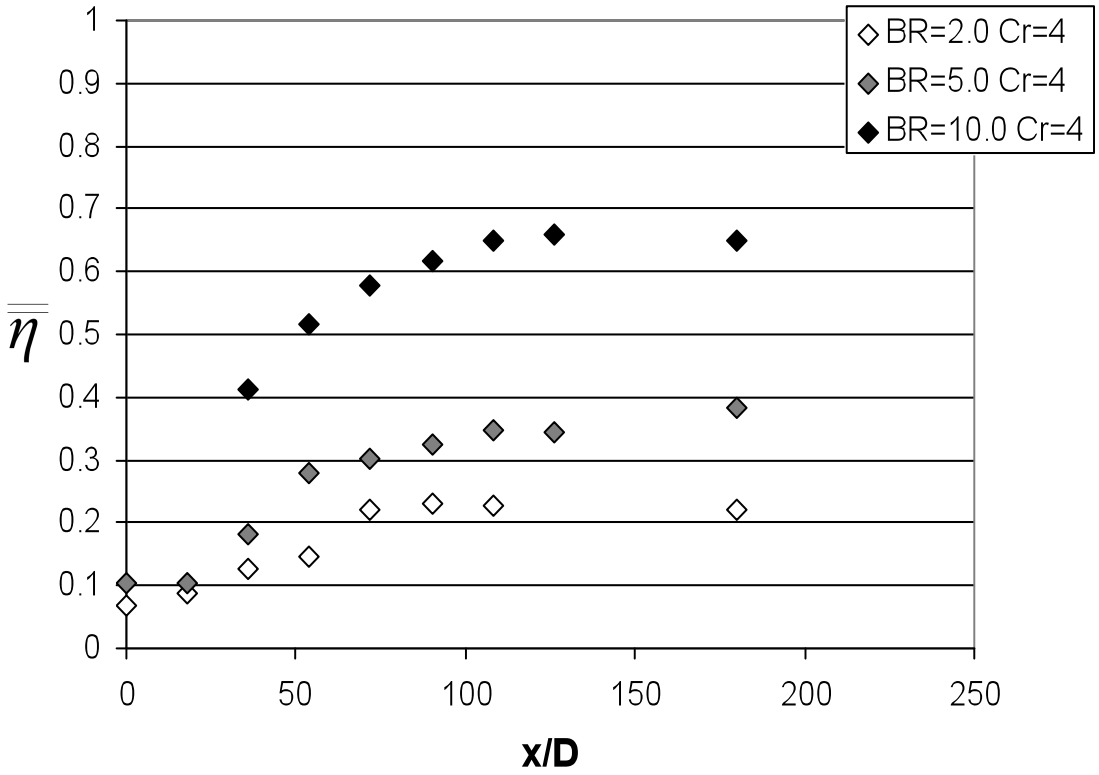

Figure 7.15. Spatially averaged effectiveness for *X/D* = 18, *Y/D* = 5, blowing ratios 2.0, 5.0, and 10.0, and a contraction ratio of 4.

7.5 Louver Experiments

A louver produces a jet of fluid parallel to the cooled surface co-directional with the bulk motion of the hot gas. This jet initially remains in contact with the surface providing a protective film. Louvers are a common feature in gas turbine combustors, so it is important to run film cooling test cases with a louver in place in order to gauge its effect. Figure 7.16 shows the affect of a louver prior to the beginning of a full array of film cooling holes. This arrangement is for $X/D = 6$, $Y/D = 5$, $Cr = 4$ and is identical to the arrangement presented in fig. 7.3 with the exception of the louver. The louver operates at a blowing ratio of 1 to minimise the generation of additional swirl which results from the joining of two fluid streams at different velocities.

A comparison between figs. 7.16 and 7.3 shows the effect of the initial film provided by the louver. This film generates high effectiveness at the beginning of the array which then quickly disperses due to turbulent mixing. It is clear that this mixing is sufficient to partially dissipate the initial film before the coolant from the holes is able to provide significant thermal protection. For each of the blowing ratios presented in fig. 7.16, the effectiveness reaches a minimum around $x/D = 12$. The figure also shows increasingly significant disruption of the initial film with increasing blowing ratio. This is because the jets produced by higher blowing ratio film cooling holes penetrate further into the freestream and generate larger kidney type vortices which then drag more hot air from the freestream into the boundary layer.

Figure 7.17 provides a comparison between the cases with the louver and those without, allowing for a more quantitative comparison. As seen in fig. 7.16, the effectiveness for the louver cases starts out relatively high, and then drops quickly.

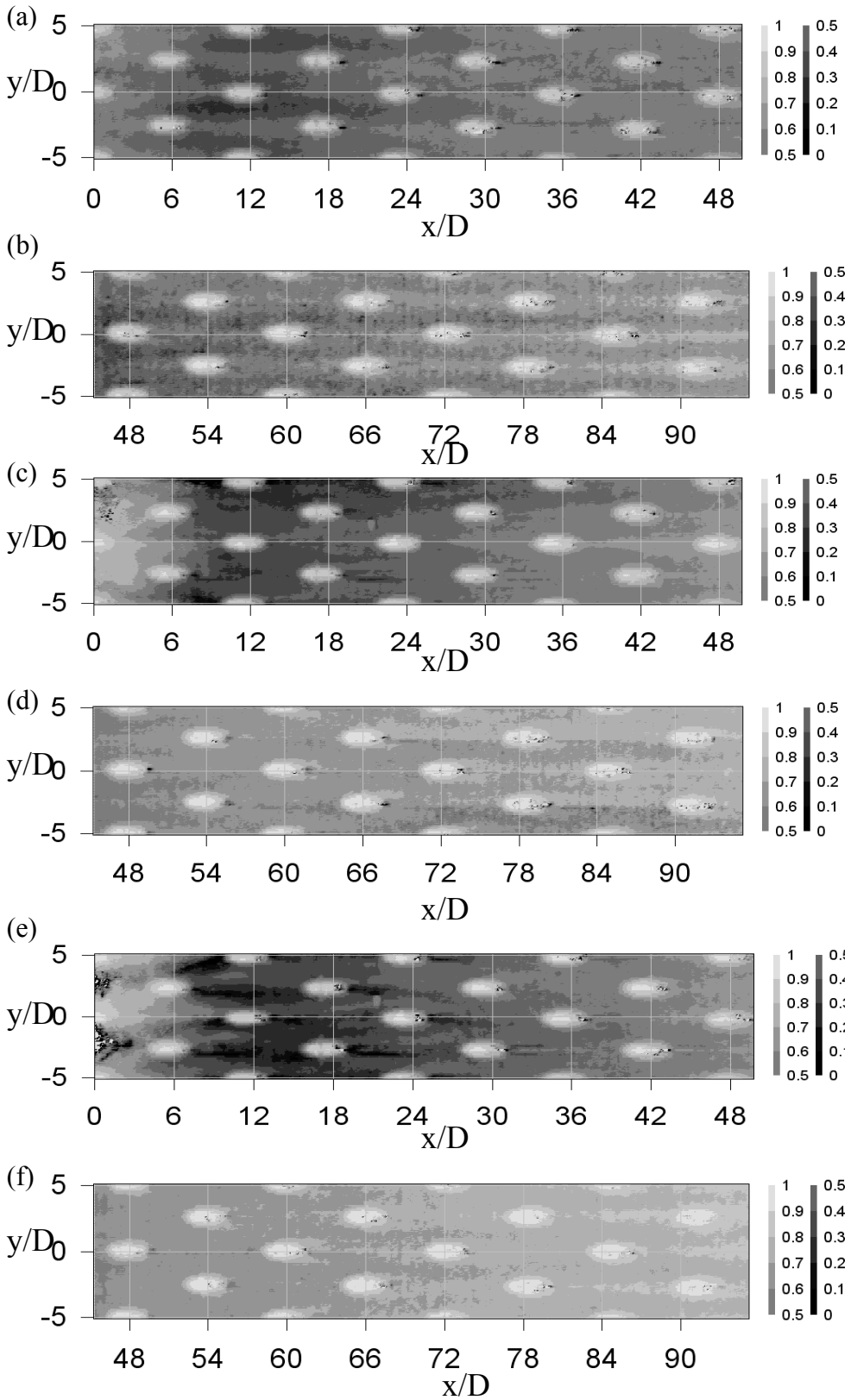

Figure 7.16. Spatially resolved effectiveness for X/D = 6, Y/D = 5 and Cr = 4 with the inclusion of a louver operating at BR = 1 and film cooling blowing ratio of (a) 2.0 from x/D = 0 to x/D = 50, (b) 2.0 from x/D = 45 to x/D = 95, (c) 5.0 from x/D = 0 to x/D = 50, (d) 5.0 from x/D = 45 to x/D = 95, (e) 10.0 from x/D = 0 to x/D = 50, and (f) 10.0 from x/D = 45 to x/D = 95.

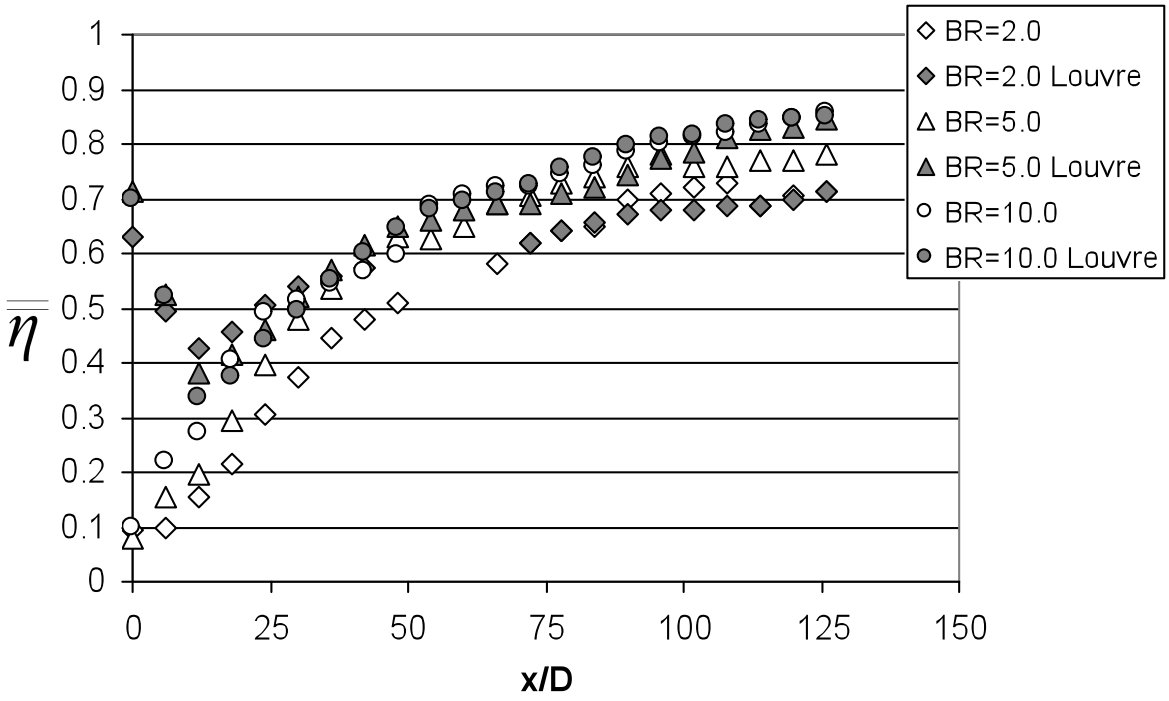

Figure 7.17. Spatially averaged effectiveness for $X/D = 6$, $Y/D = 5$ and $Cr = 4$ with the inclusion of a louver operating at $BR = 1$.

For the cases BR = 5.0 and BR = 10.0, the louver data quickly reaches the values observed for the non-louver data, and then increases gradually. The BR = 2.0 louver effectiveness data, however, remains significantly higher than the non-louver case until further along the plate. This effect takes place because the lower momentum fluid leaving the film cooling holes does not penetrate as far past the film generated by the louver and does not mix in as much hot fluid from the freestream. The end result is that the initial protective film is better preserved.

7.6 Hole Angle Comparison

Figures 7.18, 7.19, and 7.20 differ from the preceding figures in this chapter because they present effectiveness data for a test surface with film cooling holes inclined 30º to the surface rather than the 20º used in the other test surfaces. Figures 7.18 and 7.19 show spatially resolved effectiveness for hole spacing X/D = 6, Y/D = 5 and contraction ratios of 1 and 4 respectively. Just as in the cases for θ = 20º, there is essentially no difference between effectiveness values at different blowing ratios or contraction ratios, but a careful comparison with fig. 7.3 reveals that increasing the hole inclination angle delays the development of a protective film.

Figure 7.20 presents a comparison for spatially averaged effectiveness at blowing ratios of 2.0, 5.0 and 10.0 at contraction ratios of 1 and 4. This is the θ = 30º equivalent of fig. 7.11 and is surprisingly similar. In fact, the only difference is that the effectiveness values appear to have shifted roughly two row spacings to the right. This confirms the earlier observation that the steeper hole angle delays the formation of a protective film, it indicates that a small change in hole angle does not have a significant effect on an overcooled surface, and it provides further support to the observation of Lin et al. (2003) and Scrittore et al. (2007) that hole spacing is the

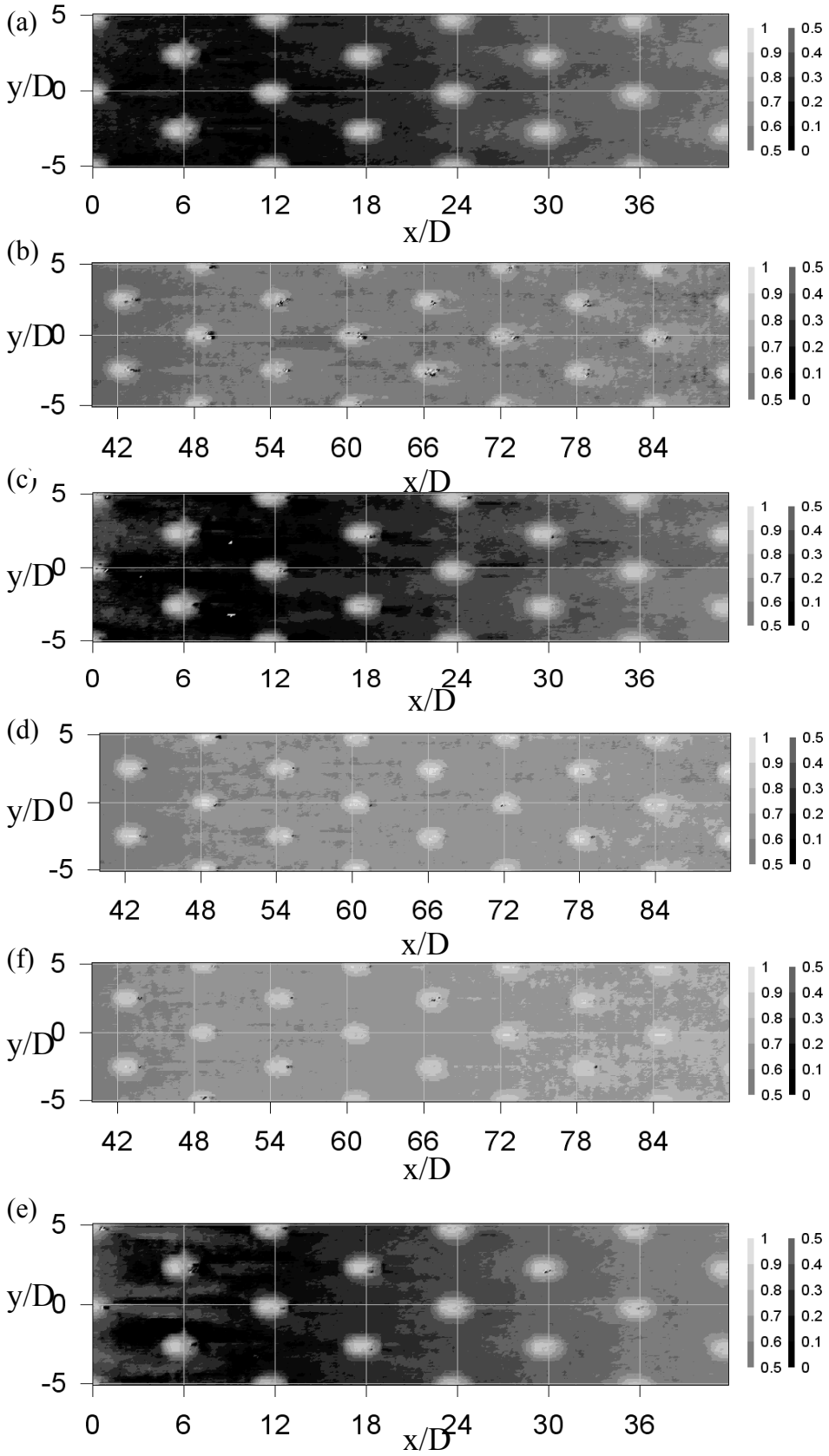

Figure 7.18. Spatially resolved effectiveness values for *X/D* = 6, *Y/D* = 5 and *Cr* = 1 for a test surface with hole inclination angle $\theta = 30^{o}$ and (a) *BR* = 2.0, *x/D* from 0 to 41 (b) *BR* = 2.0, *x/D* from 40 to 89 (c) *BR* = 5.0, *x/D* from 0 to 41 (d) *BR* = 5.0, *x/D* from 40 to 89 (e) *BR* = 10.0, *x/D* from 0 to 41 (f) *BR* = 10.0, *x/D* from 40 to 89.

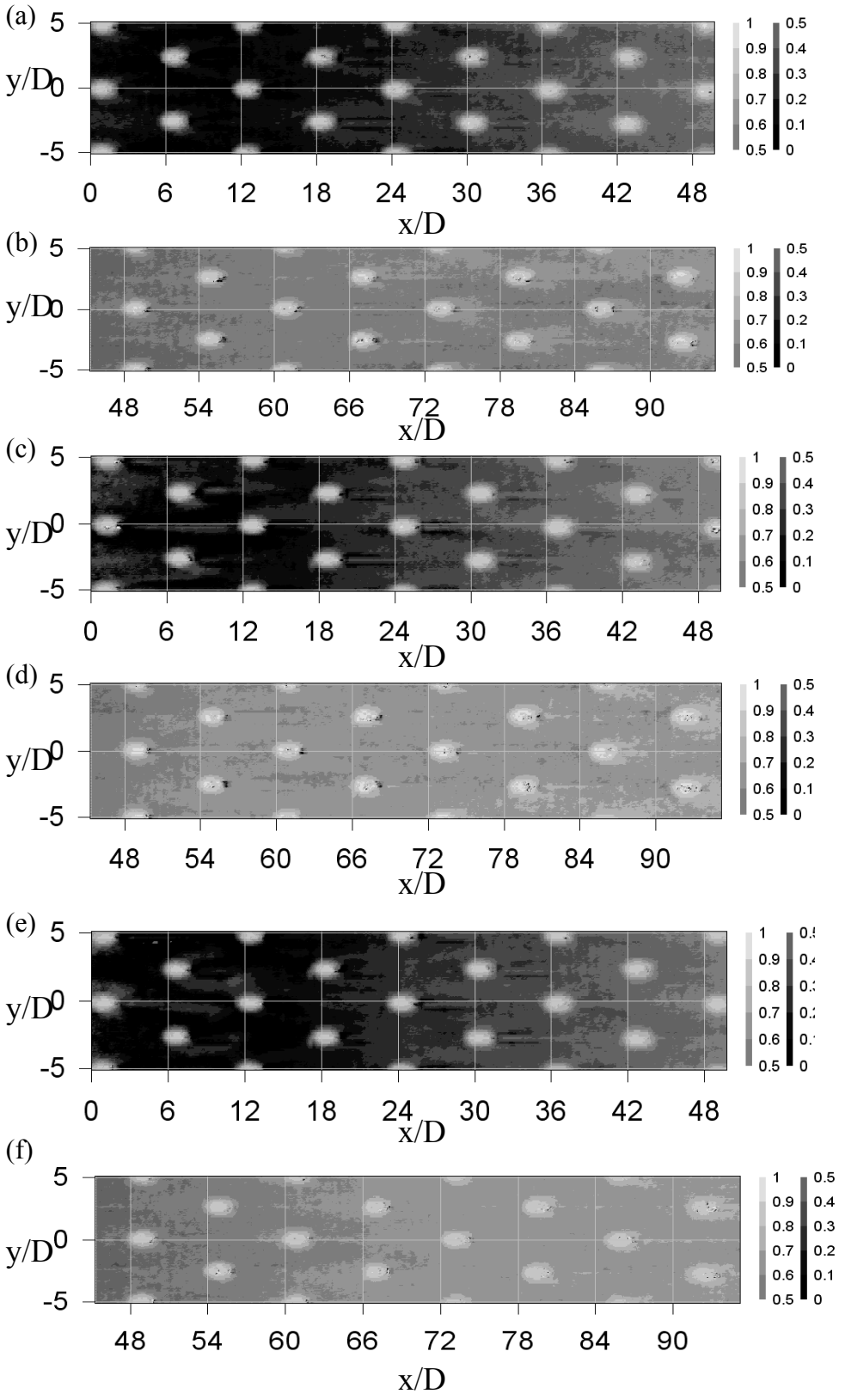

Figure 7.19. Spatially resolved effectiveness values for X/D = 6, Y/D = 5 and Cr = 4 for a test surface with hole inclination angle θ = 30º and (a) BR = 2.0, x/D from 0 to 41 (b) BR = 2.0, x/D from 40 to 89 (c) BR = 5.0, x/D from 0 to 41 (d) BR = 5.0, x/D from 40 to 89 (e) BR = 10.0, x/D from 0 to 41 (f) BR = 10.0, x/D from 40 to 89.

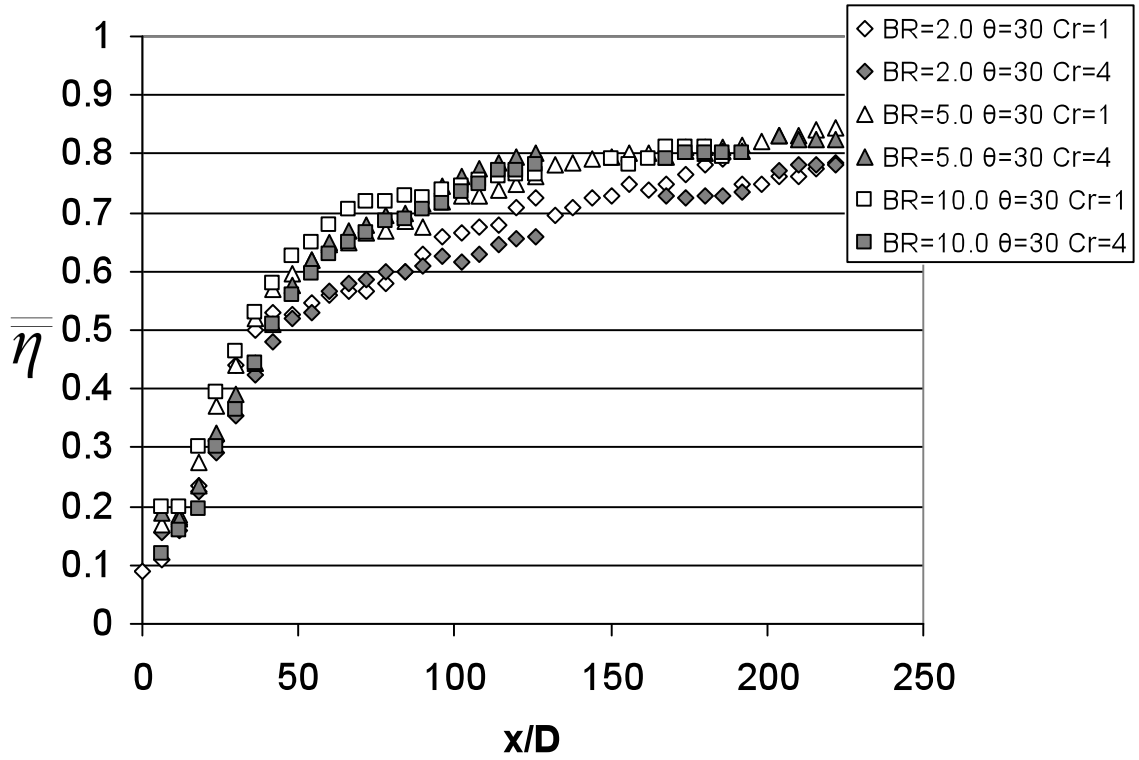

Figure 7.20. Spatially averaged effectiveness comparison plot for a test surface with hole inclination angle $\theta = 30^{\circ}$, hole spacing $X/D = 6$, $Y/D = 5$ and contraction ratios of 1 and 4.

physical parameter with the greatest effect on effectiveness for dense film cooling arrays.

7.7 Summary and Conclusions

Effectiveness data is presented for hole angle, θ = 20º and hole spacings of *X/D* = 6, *Y/D* = 3; *X/D* = 6, *Y/D* = 5; *X/D* = 6, *Y/D* = 7; and *X/D* = 18, *Y/D* = 3 at blowing ratios of 2.0, 5.0, and 10.0. Different contraction ratios are examined using values of *Cr* = 1, *Cr* = 3, *Cr* = 4, and *Cr* = 5. A test surface with hole angle, θ = 30º and hole spacing *X/D* = 6, *Y/D*=5 is used at contraction ratios of 1 and 4 to provide limited data on the affect of using different hole angles in a dense film cooling array. Limited data was also obtained using a louver with a blowing ratio of 1 to gauge its affect.

For both hole angles examined, the hole spacings *X/D*=6, *Y/D*=3; *X/D*=6, *Y/D*=5; *X/D*=6, *Y/D*=7 show only a slight increase in effectiveness when increasing the blowing ratio from 2.0 to 5.0 and no noticeable difference when increasing the blowing ratio from 5.0 to 10.0. Additionally, there is no visible dependence on contraction ratio. A lack of dependence on either blowing ratio or contraction ratio indicates a condition where excessive coolant is being injected into the combustor. This is typical of many gas turbine combustors where design simplicity is mandated by cost constraints. The high blowing ratio is a result of the pressure ratio required across the injector to generate the desired flame characteristics and mixing. The high density arrays are used to avoid high thermal gradients which would shorten the combustor's life.

Data obtained with the relatively sparse array of *X/D*=18, *Y/D*=5 appears to share the characteristics of overcooled flow seen in the denser arrays when the contraction ratio is 1. However, at *Cr*=4 blowing ratio has a large affect, with increasing effectiveness corresponding to increasing blowing ratio. This shows that

for configurations where coolant injection is not excessive, it is essential to properly account for the drop in blowing ratio along a contraction to avoid a situation with insufficient cooling.

The use of a louver to provide an initial film prevents areas of zero effectiveness in the regions around the first few rows of holes. However, at the high blowing ratios examined the early rows of film cooling holes produce jets which disturb the film and initially lower the effectiveness. For the dense array of X/D=6, Y/D=5 using a hole inclination angle of 30º has the effect of delaying the formation of a protective film because the jets protrude further into the freestream. This however, has a minimal effect on the overall effectiveness along the entire length of the film cooled surface.

Chapter 8

Summary and Conclusions

8.1 Summary

Impingement heat transfer and film cooling are essential aspects of combustor liner cooling. Prior to the present study, the effects associated with compressible impingement flows, the effect of increasing temperature ratio on impingement flows, and the effects generated by a highly variable pressure ratio along a film cooled surface have received very little attention in the available literature. This work serves to improve the understanding of combustor liner cooling by exploring these parameters.

To investigate the effect of increasing temperature ratio on impingement flows data are taken at constant Reynolds number 18,000, constant Mach number 0.2, hole spacing $X/D = 8$, $Y/D = 8$ and temperature ratios T_{wa}/T_j ranging from 1.06 to 1.73. The investigation of compressibility effects on impingement heat transfer requires holding Reynolds number constant while varying Mach number and holding Mach number constant at varying Reynolds numbers. This was done utilizing a total of 14 different test surfaces with hole diameters ranging from 3.5mm to 20mm at three different hole spacings: $X/D = 5$, $Y/D = 5$; $X/D = 8$, $Y/D = 8$; and $X/D = 12$, $Y/D = 12$. Each impingement plate has a thickness of $1D$, and the spacing between the hole exit plane and the target plate is denoted Z and is equal to $3D$. The data for the impingement investigation are given in the form of discharge coefficients, crossflow-to-jet mass flux ratios, and local, line-averaged and spatially averaged Nusselt numbers.

Film cooling effectiveness data was acquired using five different test surfaces, four different contraction ratios, three different blowing ratios, and two different

absolute velocities for each reported condition. Additionally, each combination of flow condition and physical configuration required five different tests to cover the required infrared camera views. This means that a total of 330 successful film cooling tests are reported in the film cooling results chapter. The tests plate's physical parameters are as follows: $X/D = 6$, $Y/D = 3$, $\alpha = 20^o$; $X/D = 6$, $Y/D = 5$, $\alpha = 20^o$; $X/D = 6$, $Y/D = 7$, $\alpha = 20^o$; $X/D = 18$, $Y/D = 5$, $\alpha = 20^o$; and $X/D = 6$, $Y/D = 5$, $\alpha = 30^o$. The blowing ratios used were 2.0, 5.0, and 10.0 and the contraction ratios are 1, 3, 4, and 5.

8.2 Impingement Conclusions

The examination of the effect increasing the temperature ratio T_{wa}/T_j has on local, line-averaged, and spatially-averaged Nusselt numbers reveals that Nusselt number decreases for all x/D and y/D locations for $Re_j = 18{,}000$ and $Ma = 0.2$. The spatially-averaged Nusselt number decrease is especially substantial as the T_{wa}/T_j temperature ratio increases from 1.06 to 1.73, which evidences deterioration of impingement cooling performance. The effect of increasing the temperature ratio is more apparent in the regions under the impinging jets where the heat transfer is noticeably reduced, a contrast from the surrounding areas, which show almost no change. This is believed to be due to variable property effects which degrade local turbulent transport in the impingement flow as T_{wa}/T_j increases.

Impingement data for incompressible flow where hole spacings and Reynolds number are varied to cover a wide range of conditions indicates that for each of the jet spacings, local, line-averaged, and area-averaged data show strong Reynolds number dependence. Each jet produced using $X/D = Y/D = 12$ approximates to the behaviour of an individual jet, whereas the influences of surrounding jets, including the cumulative induced cross-flows and interactions of jet-induced vortex structures, alter the

effectiveness of each individual jet when $X/D = Y/D = 8$. The interactions between adjacent jets are still stronger for $X/D = Y/D = 5$. Spatially-averaged Nusselt numbers are generally higher at closer hole spacings than values for more sparse arrays when compared at the same streamwise location. The 12*D* jet spacing data show the least variation with x/D while the 5*D* jet spacing shows the most. Comparisons of periodic line-averaged Nusselt number data show that values decrease significantly at successive x/D locations for $X/D = Y/D = 5$, whereas $X/D = Y/D = 12$ data are approximately invariant with x/D. Regardless of the Reynolds number, the qualitative local Nusselt number distributions produced by different impingement jets are similar, with good periodic repeatability in the spanwise direction for each row of streamwise impact location. Crossflow mass velocity-to-jet mass velocity ratio data are lower for sparse arrays than for dense arrays when compared at a particular value of x/D, with reasonably good agreement with the correlation of Florschuetz et al. (1981).

When considering how compressibility affects heat transfer in arrays of impinging jets, an examination of the relevant data shows that for each of the jet spacings, local, line-averaged, and area-averaged data show strong Mach number dependence, provided the impingement jet Mach number is greater than about 0.2, with increasing Mach number corresponding to an increase in Nusselt number distributions. This increase is more pronounced for tighter hole spacings, with the greatest effect seen for the $X/D = Y/D = 5$ array. The results are similar to those for incompressible flow in that each jet produced using $X/D = Y/D = 12$ approximates the behavior of an individual jet, and the influences of surrounding jets alter the effectiveness of each individual jet when $X/D = Y/D = 8$. These interactions between adjacent jets are more pronounced for $X/D = Y/D = 5$. Additionally, compressible

cases maintain the good periodic repeatability in the spanwise direction for each row of streamwise impact location as observed in the incompressible cases.

8.3 Film Cooling Conclusions

The film cooling results are easily divided into results for a dense array and results for a spare array. The dense array conditions are those with hole spacings $X/D = 6$, $Y/D = 3$; $X/D = 6$, $Y/D = 5$; $X/D = 6$, $Y/D = 7$ and hole angles of 20º and 30º. For each possible combination of dense array hole spacing, hole angle, and contraction ratio, the effectiveness shows only a slight increase when increasing the blowing ratio from 2.0 to 5.0, and there is no noticeable difference when increasing the blowing ratio from 5.0 to 10.0. This lack of dependence on either blowing ratio or contraction ratio indicates a condition where excessive coolant is being injected into the combustor. It is of note that the effectiveness does not improve with increasing blowing ratio past a maximum value at a given x/D location for each hole spacing considered. When a louver operating at a blowing ratio of 1 was used with hole spacing $X/D = 6$, $Y/D = 5$ and contraction ratio 4, an initial film was observed, preventing areas of zero effectiveness in the regions around the first few rows of holes. However, at the high blowing ratios examined the early rows of film cooling holes produce jets which disturb the film and initially lower the effectiveness.

In contrast to the trend of insensitive effectiveness values observed for dense arrays, film cooling data for the relatively sparse array of $X/D = 18$, $Y/D = 5$ shows strong variations with both contraction ratio and blowing ratio. When considering a contraction ratio of 1, the data obtained with the $X/D = 18$, $Y/D = 5$ test surface appears to share the characteristics of overcooled flow seen in the denser arrays. However, at $Cr = 4$ blowing ratio has a large affect, with increasing effectiveness corresponding to increasing blowing ratio.

The film cooling results serve to improve the understanding of combustor liner film cooling. They verify that even though contraction ratio does not have a significant effect for overcooled combustor liners, it must be taken into account for leaner systems to prevent insufficient cooling. Additionally, all the film cooling data herein presented adds to the body of published film cooling data, providing engineers and scholars with information that can be used as a basis for further research or to calibrate numerical and computational models.

8.4 Future Work

The correlations developed as part of the impingement portion of the study, while useful, are each limited to a relatively small range of conditions. It is possible that a single correlation equation could be developed that accounts for both Mach number and temperature ratio effects over a wider range of conditions. To do this, researchers must first increase the number of available data sets, particularly for the temperature ratio. It will then be necessary to organize the results in such a way that a single correlation based on hole spacing, temperature ratio, Reynolds number, and Mach number can be developed, similar to the correlation of Florschuetz et al. (1981) which is based only on Reynolds number and hole spacing.

The film cooling work reported here is almost entirely for conditions with excessive coolant flow. This means that more coolant is used than is required to meet the measured effectiveness values. It would be useful find the blowing ratio at which no further improvement in effectiveness occurs for a range of hole spacings. Future work in this area would be focused on finding this “maximum” value. For example: at hole spacing $x/D = 5$, $y/D = 12$, there is a point where increasing the blowing ratio no longer improves effectiveness over the entire array. If this point were found for a

wide range of hole spacing configurations, it should then be possible to develop a simple correlation between maximum effective blowing ratio and hole spacing.

Appendix A

Bibliography

Abreu, M.E., Virenda, M.S., 1998, "Impingement/Effusion Cooled Combustor Liner," United States Patent Number 5,758,504.

Anthony, R.J., Oldfiend, M.L.G., Jones, T.V., and LaGraff, J.E., 1999, "Development of High-Density Arrays of Thin Film Heat Transfer Gauges," JSME Thermal Engineering Joint Conference AJTE99-6159.

Anthony, R.J., Jones, T.V., and LaGraff, J.E., 2005, "High Frequency Surface Heat Flux Imaging of Bypass Transition," Journal of Turbomachinery, **127**, pp. 241-250.

Bailey, J. C., Bunker, R. S., 2002, Local Heat Transfer and Flow Distributions for Impinging Jet Arrays of Dense and Sparse Extent, ASME Paper No. ASME GT-2002-30473.

Baldauf S., Schultz A., Wittig S., 2001, "High-Resolution Measurements of Local Effectiveness From Discrete Hole Film Cooling," Journal of Turbomachinery, **123**, pp. 758-765.

Baldauf S., Schultz A., Wittig S., 2001, "High-Resolution Measurements of Local Heat Transfer Coefficients From Discrete Hole Film Cooling," Journal of Turbomachinery, **123**, pp. 749-757.

Barigozzi, G., Benzoni, G., Franchini, G., and Perdichizzi, A., 2006, "Fan-Shaped Hole Effects on the Aero-Thermal Performance of a Film-Cooled Endwall," Journal of Turbomachinery, **128**, pp. 43-51.

Bhargava, R.K., Bianchi, M., Campanari, S., De Pascale, A., Di Montenegro, G.N., Peretto, A., 2008, "High Efficiency Gas Turbine Based Power Cycles – A Study of the Most Promising Solutions: Part 1 – A Review of the Technology," ASME Turbo Expo 2008.

Brevet P., Dejeu C., Dorignac E., Jolly M., and Vullierme J. J., 2002, "Heat Transfer to a Row of Impinging Jets In Consideration of Optimization," International Journal of Heat and Mass Transfer, **45**, pp. 4191-4200.

Brevet P., Dorignac E., and Vullierme J. J., 2001, "Mach Number Effect On Jet Impingement Heat Transfer," Heat Transfer in Gas Turbine Systems, Annals of the New York Academy of Sciences, **934**, pp. 409-416.

Bunker R., and Metzger D. E., 1990, "Local Heat Transfer In Internally Cooled Turbine Airfoil Leading Edge Regions: Part I – Impingement Cooling Without Film Extraction," ASME Transactions-Journal of Turbomachinery, **112**, pp. 451-458.

Burd, S.W., and Simon, T.W., 1997, "The Influence of Coolant Supply Geometry on Film Coolant Exit Flow and Surface Adiabatic Effectiveness," ASME Paper 97-GT-25

Chance J. L., 1974, "Experimental Investigation of Air Impingement Heat Transfer Under an Array of Round Jets," TAPPI, **57**, No. 6, pp. 108-112.

Coulthard, S.M., Volino, R.J., Flack, K.A., 2006, "Effect of unheated Starting Lengths on Film Cooling Experiments," Journal of Turbomachinery, **128**, pp. 579-588.

Diakunchak, I., Kiesow, H.J., McQuiggan, G., 2008, "The History of the Siemens Gas Turbine," ASME Turbo Expo 2008.

Downs, S. J., James, E. H., 1987, Jet Impingement Heat Transfer - A Literature Survey, ASME Paper No. 87-HT-35.

Epstein, A. H., Kerrebrock, J. L., Koo, J. J., Preiser, U. Z., 1985, Rotational Effects on Impingement Cooling, Symposium on Transport Phenomena in Rotating Machinery, Honolulu.

Florschuetz L. W., Truman C. R., and Metzger D. E., 1981, "Streamwise Flow and Heat Transfer Distributions for Jet Array Impingement With Crossflow," ASME Transactions–Journal of Heat Transfer, **103**, pp. 337-342.

Fox M. D., Kurosaka M., Hedges L., and Hirano K., 1993, "The Influence of Vortical Structures on the Thermal Fields of Jets," Journal of Fluid Mechanics, **255**, pp.447-472.

Gauntner, J.W., Livingood, N.B., and Hrycak, P., 1970 "Survey of Literature on Flow Characteristics of a Single Turbulent Jet Impinging on a Flat Plate," Nasa Techical Note D-5652

Goldstein, R.J., and Eckert, E.R.G., 1974, "Effects of Hole Geometry and Density on Three-Dimensional Film Cooling," International Journal of Heat and Mass Transfer, **17**, pp. 595-607.

Goodro M., Park J., Ligrani P.M., Fox M., Moon H.-K., 2007, "Effects of Mach Number and Reynolds Number on Jet Array Impingement Heat Transfer," International Journal of Heat and Mass Transfer, **50**, pp. 367-380

Gritsch, M., Schulz, A., Wittig, S., 2000, "Film-Cooling Holes with Expanded Exits: Near-Hole Heat Transfer Coefficeints, International Journal of Heat and Fluid Flow," **21**, pp. 145-155.

Gritsch, M., Schulz, A., and Wittig, S., 2001, "Effect of Crossflows on the Discharge Coefficient of Film Cooling Holes with Varying Angles of Inclination and Orientation," Journal of Turbomachinery, **123**, pp. 781-787.

Guo, S.M., Lai, C.C., Jones, T.V., Oldfield, M.L.G., Lock, G.D, and Rawlinson, A.J., 2000, "Influence of Surface Roughness on Heat Transfer and Effectiveness for fully Film Cooled Nozzle Guide Vane Measured by Wide Band Liquid Crystals and Direct Heat Flux Gauges," Journal of Turbomachinery, **122**, pp. 709-716.

Jambunathan, K., Lai, E., Moss, M. A., Button, B. L., 1992, A Review of Heat Transfer Data for Single Circular Jet Impingement, International Journal of Heat and Fluid Flow, **13** (2), pp. 106-115.

Johnson, D. G., 1985, "Norwegian gas turbine pioneer: Aegidius Elling.," Energy World, pp. 10-12.

Kercher D. M., and Tabakoff W., 1970, "Heat Transfer By a Square Array of Round Air Jets Impinging Perpendicular to a Flat Surface Including the Effect of Spent Air," ASME Transactions-Journal of Engineering for Power, **92**, pp. 73-82.

Kline, S. J., and McClintock, F. A., 1953, "Describing Uncertainties in Single Sample Experiments," Mechanical Engineering, **75**, pp. 3-8.

Leger, B., Miron, P., Emidio, J.M., 2002, "Geometric and Aero-Thermal Influences on Multiholed Plate Temperature: Application on Combustor Wall," International Journal of Heat and Mass Transfer, **46**, pp. 1215-1222.

Li, X., Gaddis, J. L., Wang, T., 2002, Mist/Stream Heat Transfer with Jet Impingement onto a Concave Surface, ASME Paper No. GT-2002-30475.

Lin, Y., Song, B., Li, B., Liu, G., Wu, Z., 2003, "Investigation of Film Cooling Effectiveness of Full-Coverage Inclined Multihole Walls with Different Hole Arrangements," ASME Paper Number GT-2003-38881.

Ling, J.P.C.W., Ireland, P.T., Turner, L., 2002, "Full Coverage Film Cooling for Combustor Transition Sections," ASME Paper Number GT-2002-30528.

Mattern, C., Hennecke, D. K., 1996, Influence of Rotation on Impingement Cooling, ASME Paper No. GT-1996-161.

Mayle, R.E., Camarata, F.J., 1975, "Multihole Cooling Film Effectiveness and Heat Transfer," Journal of Heat Transfer, **97** (4), pp. 534-538.

Metzger D. E., Florschuetz L. W., Takeuchi D. I., Behee R. D., and Berry R. A., 1979, "Heat Transfer Characteristics for Inline and Staggered Arrays of Circular Jets With Crossflow of Spent Air," ASME Transactions-Journal of Heat Transfer, **101**, pp. 526-531.

Metzger D. E., and Korstad R., 1972, "Effects of Crossflow On Impingement Heat Transfer," ASME Transactions-Journal of Engineering for Power, **94**, pp. 35-41.

Moffat, R. J., 1988, "Describing the Uncertainties in Experimental Results," Experimental Thermal and Fluid Science, **1** (1), pp. 3-17.

Obot N. T., and Trabold T. A., 1987, "Impingement Heat Transfer Within Arrays of Circular Jets: Part 1-Effects of Minimum, Intermediate, and Complete Crossflow for Small and Large Spacings", ASME Transactions-Journal of Heat Transfer, **109**, pp. 872-879.

O'Dowd, D., Zhang, Q., Ligrani, P., He, L., Friedrichs, S., 2009, "Comparison of Six Heat Transfer Techniques to Measure Heat Transfer Characteristics on Turbine Blade Tips," ASME Paper Number GT-2009-59376.

Oldfield, M.L.G.., 2008, "Impulse Response Processing of Transient Heat Transfer Gauge Signals," Journal of Turbomachinery, 130, pp. 021023-1 – 021023-9.

Park J., Goodro M., Ligrani P. M., Fox M., Moon H.-K., 2007, "Separate Effects of Mach Number and Reynolds Number on Jet Array Impingement Heat Transfer," Journal of Turbomachinery, **129**, pp. 269-280

Parsons, J. A., Han, J. C., Lee, C. P., 1996, Rotation Effect on Jet-Impingement Heat Transfer in Smooth Rectangular Channels with Four Heated Walls and Radial Crossflow, ASME Transactions-Journal of Turbomachinery, **120**, 79-85.

Parsons, J. A., Han, J. C., 2001, Rotation Effect on Jet Impingement Heat Transfer in Smooth Rectangular Channels with Coolant Extraction, International Journal of Rotating Machinery, **7**, 87-103.

Parsons, J. A., Han, J. C., Lee, C. P., 2003, Rotation Effect on Jet-Impingement Heat Transfer in Smooth Rectangular Channels with Four Heated Walls and Coolant Extraction, ASME Paper Number GT-2003-38905.

Roach, P.E., 1986, "The Generation of Nearly Isotropic Turbulence by Means of Grids," Journal of Heat and Fluid Flow, **8** (2), pp. 82-92.

San, J.-Y., Lai, M.-D., 2001, Optimum Jet-to-Jet Spacing of Heat Transfer for Staggered Arrays of Impinging Air Jets, International Journal of Heat and Mass Transfer, **44**, pp. 3997-4007.

Sasaki, M., Takahara, K., Kumagai, T., Hamano, M., 1979, "Film Cooling Effectiveness for Injection from Multirow Holes," Journal of Engineering for Power, **101**, pp. 101-108.

Saumweber, C., Schulz, A., 2004, "Interaction of Film Cooling Rows: Effects of Hole Geometry and Row Spacing on the Cooling Performance Downstream of the Second Row of Holes," Journal of Turbomachinery, **126**, pp. 237-246.

Scrittore, J.J., Thole, K.A., Burd, S.W., 2007, "Investigation of Velocity Profiles for Effusion Cooling of a Combustor Liner," Journal of Turbomachinery, **129**, pp. 518-526.

Taslim, M. E., Pan, Y., Bakhtari, K., 2002, Experimental Racetrack Shaped Jet Impingement on a Roughened Leading-Edge Wall with Film Holes, ASME Paper Number GT-2002-30477.

Van Der Linden, S., 1988, “The World’s First Industrial Gas Turbine Set at Neuchâtel (1939),” ASME International Historic Mechanical Engineering Landmark, Neuchâtel, Switzerland.

Viskanta, R., 1993, Heat Transfer to Impinging Isothermal Gas and Flame Jets, Experimental Thermal and Fluid Science, **6**, pp. 111-134

Waye, S.K., Bogard, D.G.., 2007, “High-Resolution Film Cooling Effectiveness Comparison of Axial and Compound Angle Holes on the Suction Side of a Turbine Vane,” Journal of Turbomachinery, **129**, pp. 202-211.

Yuen, C.H.N., Martinez-Botas, R.F., 2005, “Film Cooling Characteristics of Row of Round Holes at Various Streamwise Angles in a Crossflow: Part I. Effectiveness,” International Journal of Heat and Mass Transfer, **48**, pp. 4995-5016.

Appendix B

Software Directory

Table B.1. Listing of data analysis programs and their uses for the impingement study.

software	description
LabView	Used for all data acquisition and to determine impingement mass flow rate, hole Reynolds number, mean hole velocity, impingement correction factor, jet stagnation temperature, and jet static pressure
Excel	Generates IR calibration equations using IR image data and thermocouple data, also used to organize data into line-average and spatially-averaged plots
Matlab	Extracts grey scale data from IR images, calculates temperatures, calculates Nusselt numbers, and exports data files
Tecplot	Generates spatially-resolved Nusselt number distributions from data files produced by Matlab
Fortran	Produce analytical predictions based on Florscheutz's equation [5], and calculates both predicted and actual discharge coefficients

Table B.2. Listing of data analysis programs and their uses for the film cooling study.

software	description
LabView	Used to acquire signals from thermocouples, pressure transducers and to record IR video. Also performed limited calculations to determine louver plowing ratio in limited cases
Excel	Determines blowing ratio distributions, produces IR calibration equations using IR image data and thermocouple data, and generates spatially-averaged effectiveness plots
Matlab	Imports IR video files generated using LabView, producing adiabatic wall temperatures and effectiveness data files using IR calibration equations calculated with Excel and the impulse response method
DPlot	Generates spatially-resolved effectiveness distributions from data files produced by Matlab

Appendix C

Uncertainty Analysis

Appendix C contains the uncertainty analysis results, which were determined using procedures described by Kline and McClintock [43] and by Moffat [44].

Table C.1. Uncertainty analysis result.

Variable	Unit	Uncertainty
Temperature	ºC	± 0.15
IR Spatial Resolution	mm	± 0.2
IR Temperature Resolution	ºC	± 0.4
Local Nusselt Number	%	± 4.8
RF	%	± 2.4
T_{aw}	ºC	± 0.5
Re_j	%	± 2.0 for Re_j=20,000
η_{aw} using impulse response method	%	± 5.0

Appendix D

Impingement Target Plate Iterations

Appendix D contains a description of the development procedure of the target plates used in the present study. Figure D.1 represents the first heated target plate developed for the study. It was constructed using 0.0625" polycarbonate, ten copper-constantan thermocouples, clear epoxy, and a 10" x 10" Kapton® Thermofoil® heater. It proved impractical because the uneven thermal expansion of the polycarbonate caused unacceptable warping. Successive target plates were constructed using 0.050" polycarbonate plates which corrected the problem. Figure D.2 shows a target plate with a fractured polycarbonate plate. The fracture was caused by excessive pressure exerted by high speed impingement jets. Figure D.4 is manufactured using the same methods and materials as the target plate in fig D.2, the exceptions being that it is one half the width and is set in a frame reinforced with T-section acrylic pieces. This adequately compensates for the pressure associated with high speed impingement jets. Figure D.5 shows an instrumented, standard dimension target plate (10" x 10") properly mounted on the impingement plenum, with an impingement plate visible behind it.

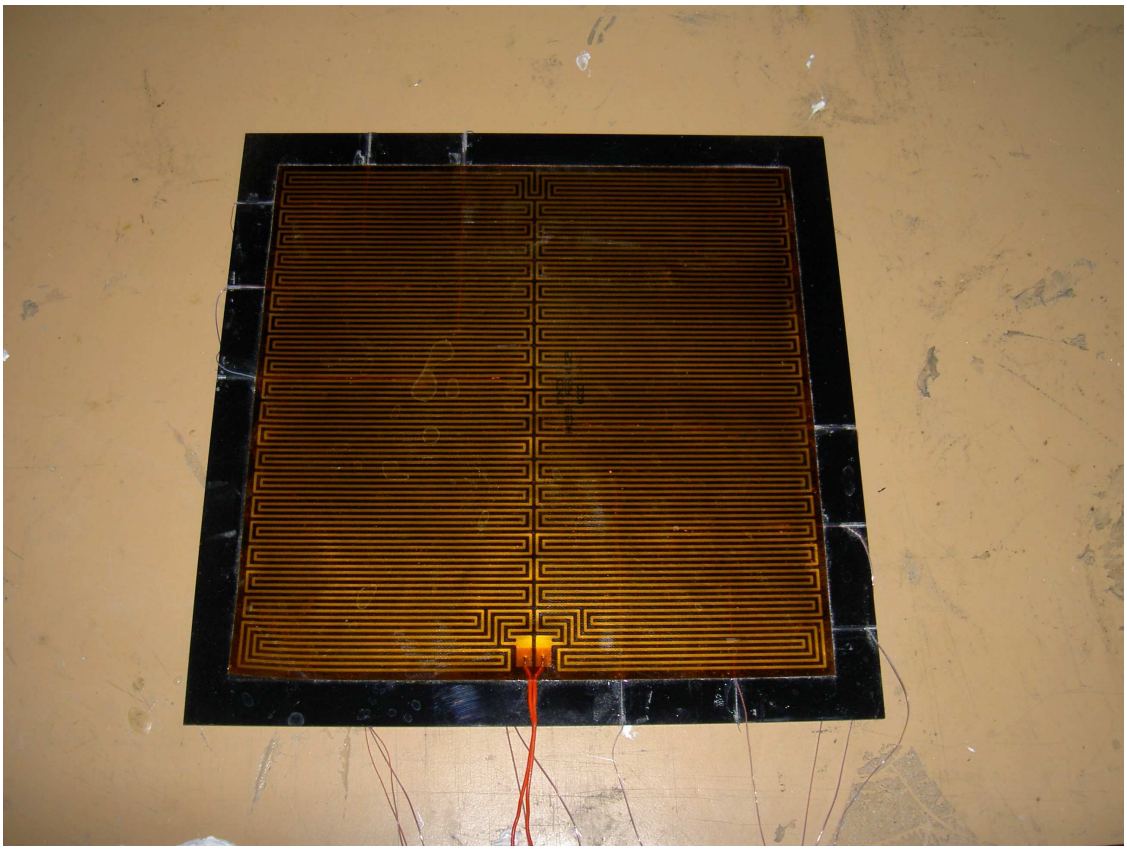

Figure D.1. First Target Plate Iteration measuring 0.28 m x 0.28 m.

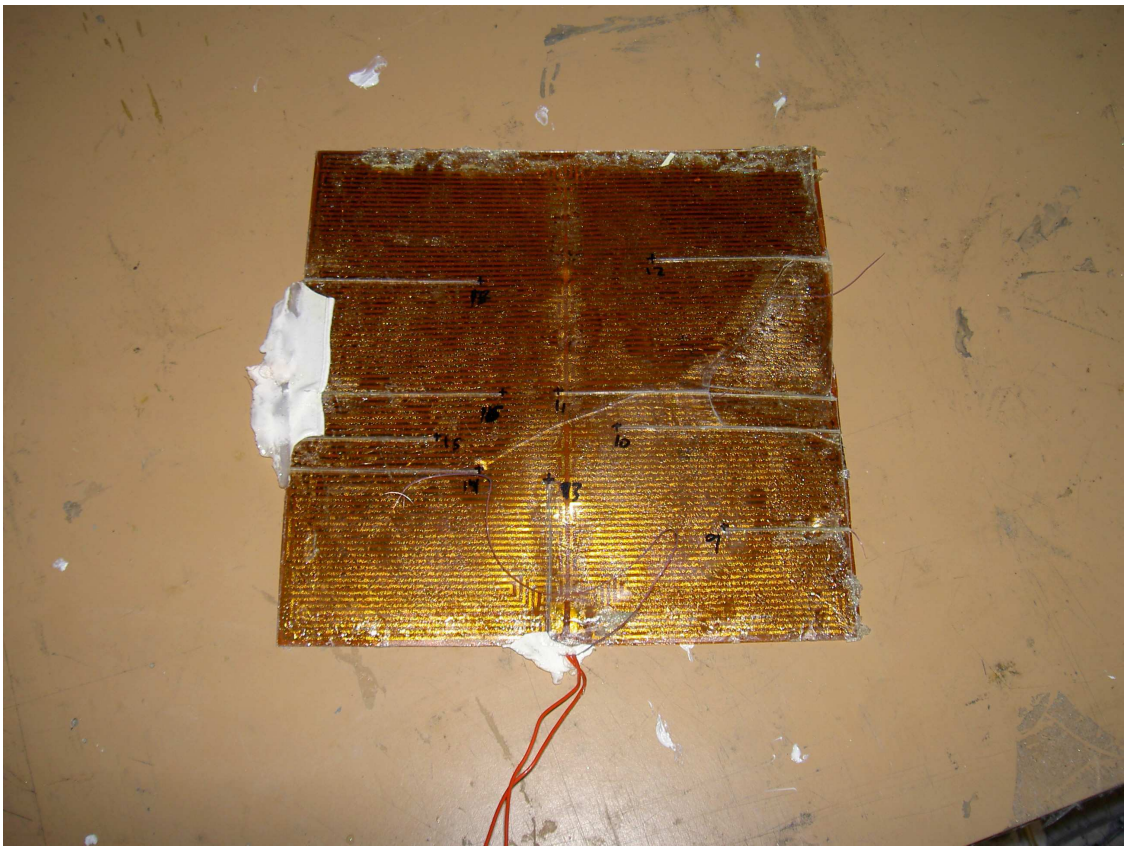

Figure D.2. Pressure Damaged Target Plate at 0.25 m x 0.25 m.

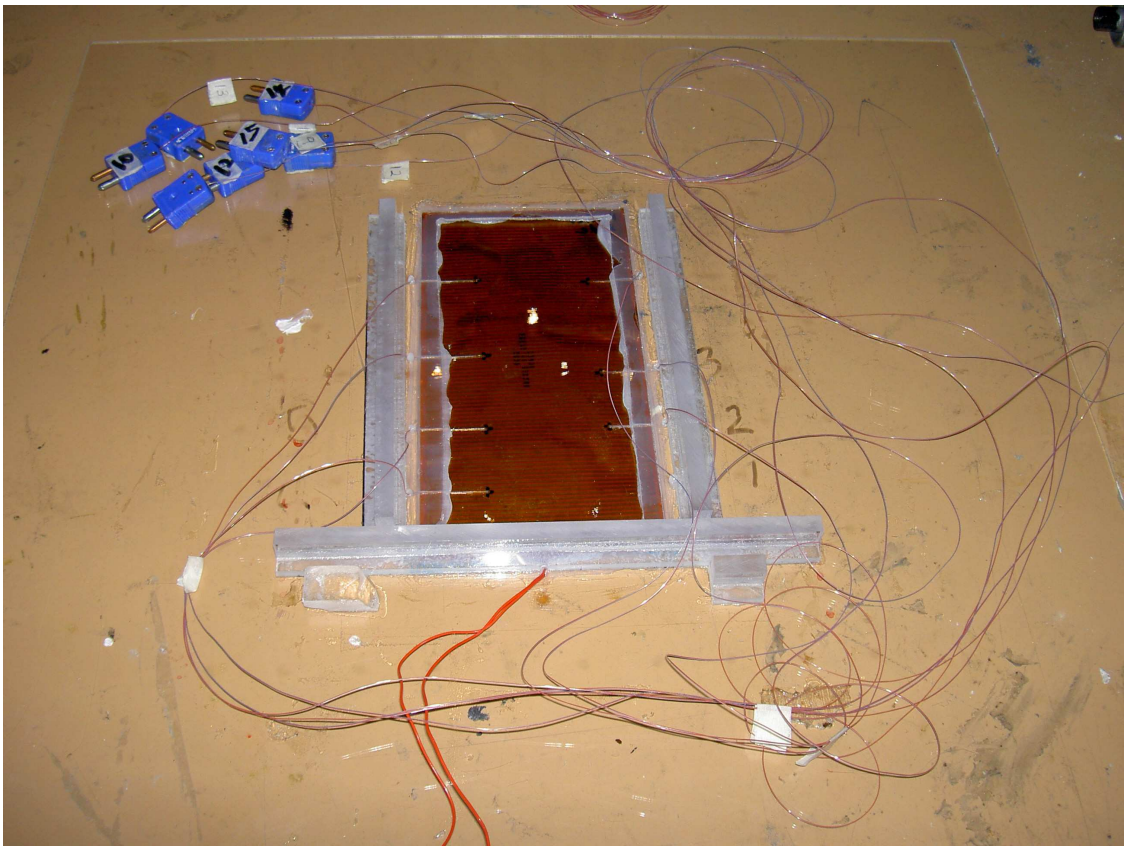

Figure D.4. Target Plate for Use with High Speed Impingement Jets, 0.25 m x 0.13 m.

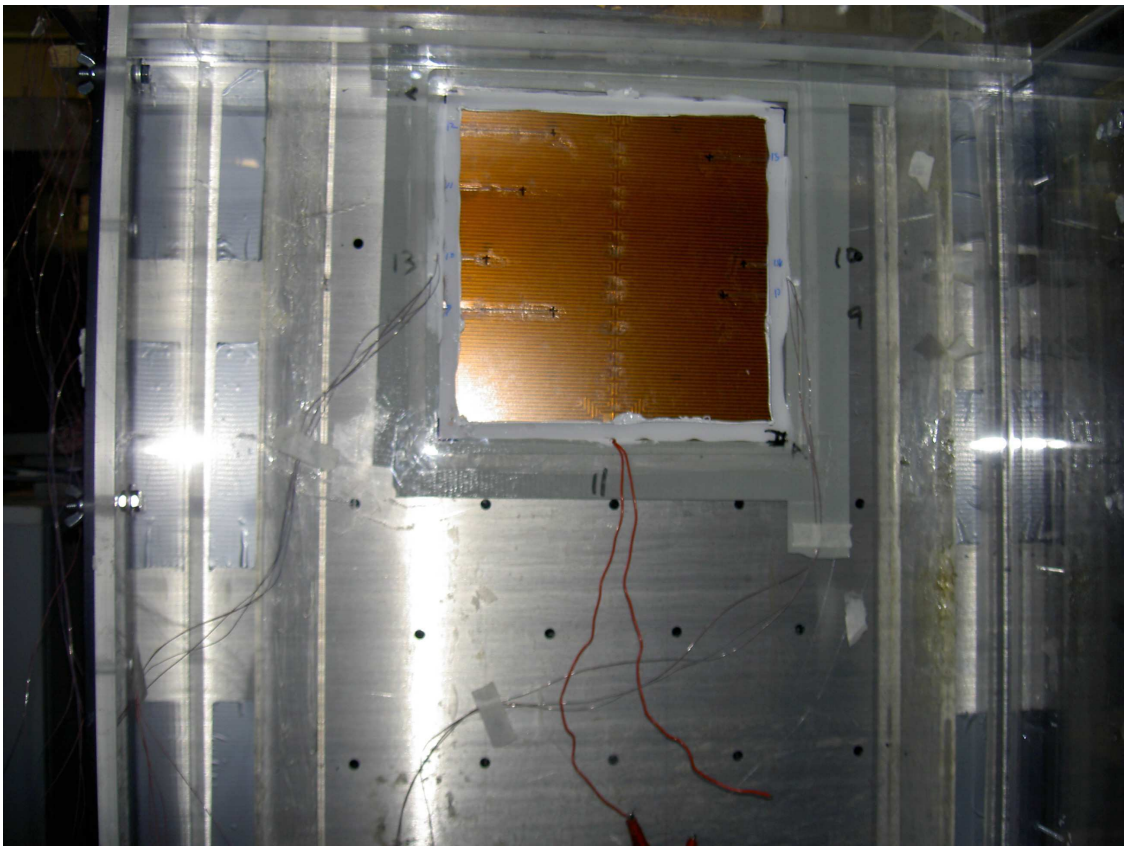

Figure D.5 Target Plate Properly Mounted on Impingement Plenum.